Sensitivity of Boundary Layer Ingestion Effects to Tube and Wing Airframe Design Features

Jai Ahuja* and Dimitri N. Mavris [†]

Aerospace Systems Design Laboratory, School of Aerospace Engineering,
Georgia Institute of Technology, Atlanta, GA, 30332, USA

Conceptual design of boundary layer ingesting (BLI) aircraft requires a methodology that captures the aero-propulsive interactions in a parametric fashion. This entails modeling the impacts of BLI as a function of the airframe and propulsor design. Previous work has analyzed the sensitivity of these BLI effects to the propulsor size and throttle. This paper assesses the sensitivity of the BLI effects to the airframe design through a series of experiments, using CFD. The scope of this analysis is restricted to tube and wing type BLI concepts. Results from these studies help identify the critical airframe design space that needs to be considered when generating a parametric model of the BLI effects. Guidelines regarding the level of detail required for the airframe geometry model are discussed.

I. Nomenclature

Symbols

A	Area
$C_{\dot{E}}$	Non dimensional change in wake dissipation
C_p	Pressure coefficient
$C_{P_{K_{in}}}$	Non dimensional $P_{K_{in}}$
D	Drag
$\dot{E}$	Total mechanical energy flow rate out of the control volume boundary
F_N	Net momentum flux across propulsor (net thrust for non-BLI engine)
F_X	Net axial force on aircraft
L	Length
$\dot{m}$	Mass flow rate
M	Mach number
$\hat{\mathbf{n}}$	Unit normal vector for a control volume boundary surface
p	Static pressure
P_K	Net mechanical power added to the flow by the propulsor
$P_{K_{in}}$	P_K evaluated at propulsor inlet
$P_{K_{out}}$	P_K evaluated at propulsor outlet
p_t	Total pressure

S	Planform area
S_B	Control volume boundary on airframe surface
S_O	Control volume outer boundary
S_{ref}	Reference area for non-dimensional coefficients
S_{TP}	Trefftz Plane
u	Perturbation velocity in the x direction
$\left(\frac{t}{c}\right)_{max}$	Maximum airfoil thickness to chord
v	Perturbation velocity in the y direction
$\mathbf{V}$	Velocity vector
V	Flow velocity magnitude
w	Perturbation velocity in the z direction

Greek

α	Angle of attack
β	Symbol representing all BLI effects
Γ	Dihedral
δ	Boundary layer thickness
η_{PR}	Pressure recovery
θ	Circumferential location of engine on fuselage
λ	Taper ratio

Λ_{LE}	Leading edge sweep angle
ρ	Static density
ϕ	Inlet angle
Φ	Total dissipation
Φ_{afm}	Total dissipation contribution from the airframe: $\Phi - \Phi_{jet}$
Φ_{jet}	Propulsor jet mixing dissipation
Φ_{surf}	Dissipation in aircraft surface boundary layers
Φ_{vortex}	Dissipation in aircraft trailing vortex sheet
Φ_{wake}	Dissipation in aircraft wake
ψ	Inlet skinning angle

Engine Station Numbers

0	Ambient
1	Inlet highlight plane
2	Fan face
19	Bypass nozzle exit plane
9	Core nozzle exit plane

Conventions

$(\cdot)'$	Non-BLI quantities
$(\cdot)_\infty$	Freestream quantities
$(\cdot)_v$	Vertical tail parameters
$A(\cdot)C(\cdot)$	Axial and circumferential location of measurement station

---

*PhD Candidate, Aerospace Systems Design Laboratory, Georgia Institute of Technology, AIAA Student Member
[†]S.P. Langley Distinguished Regents Professor, Georgia Institute of Technology, AIAA Fellow

II. Introduction

Economic and environmental benefits of fuel efficient aircraft have driven research towards unconventional configurations and technologies. Boundary Layer Ingesting (BLI) aircraft concepts such as the N3-X Turboelectric Distributed Propulsion (TeDP) Blended Wing Body (BWB) [1, 2], STARC-ABL [3], D8 Double Bubble [4–6], and the Onera NOVA-BLI [7], for example, appear to be promising solutions, relying on a synergistic interaction between the airframe and propulsor for improved fuel efficiency. Maximizing benefits of BLI while minimizing the risks not only involves careful design of the propulsor, but also the airframe given that the embedded propulsor performance is dependent on the ingested boundary layer flow, which in turn is affected by the airframe. The highly coupled nature of the propulsion system with the airframe for BLI concepts requires a Multidisciplinary Design Analysis and Optimization (MDAO) approach.

To formulate a coupled aero-propulsive design methodology for the airframe and engine at the conceptual design stage, where design knowledge is limited, the impacts of BLI need to be considered in a parametric fashion. In other words, the impacts of BLI on the vehicle performance must be considered as a function of the airframe and propulsor design, and operating conditions, such that trade space exploration to enable growth in design knowledge is possible, while accounting for the key physics unique to such concepts, at every design combination. Limitations of low fidelity aerodynamics models for capturing complex physics like shocks, 3D boundary layer features, flow separation, and other transonic flow effects that have a significant influence on the vehicle design, motivate the need for CFD to augment aerodynamics modeling at the conceptual design stage for BLI aircraft.

A challenge with using CFD in early conceptual design is the level of airframe geometry detail that one needs to consider to obtain performance estimates for a vehicle. Metrics like drag, lift, pitching moment, etc. are rather sensitive to details like fairings, fuselage nose contours, etc. in addition to the usual candidates like airfoils, planform shape, etc. The dimensionality of the problem is thus opened up considerably when using CFD for performance analysis than when using lower fidelity aerodynamics models. It is not very practical to define detailed airframe contour parameters like spline fit coefficients and vehicle sizing parameters at the same time, since the latter require aerodynamics analysis at all points in the mission profile, something that is too expensive with CFD, while the former cannot always be appropriately modeled using lower fidelity aerodynamics models. For this reason, low fidelity approaches have traditionally been used for vehicle sizing, with CFD used for detailed design and analysis once a few promising baselines have been established.
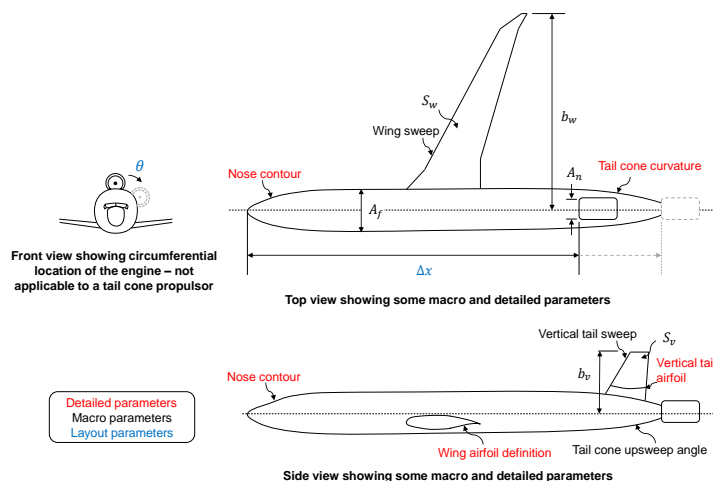
With BLI, as discussed before, there is a need for CFD analysis at the very early stages of design. If one restricts the modeling scope to just capturing the ingested boundary layer characteristics relevant for a given design/analysis problem, then what features of the airframe geometry outer mold line (OML) and external layout need to be considered when generating a parametric representation of these BLI effects using CFD in conceptual design, and what features can be defaulted? This is the overarching research question to be answered. Studies that have used CFD generated profiles as inputs for a given analysis have not commented on this aspect. Florea [8], Hardin [9], and Felder [2], obtained profiles from Boeing's CFD analysis of the BWB, while Welstead [3] used Boeing's SUGAR CFD analysis to obtain representative profiles for the STARC-ABL conceptual design. Other studies like those by Liu [10] used profiles from a fixed geometry similar to the N3X, while Lee [11] obtained baseline inlet geometry from Boeing, but used a flat plate to model the airframe. The study by Kenway and Kiris [12] provides some insight into the impacts of geometry detail on the boundary layer characteristics. They found that wing downwash had an impact on the distortion pattern at the BLI propulsor Aerodynamic Interface Plane (AIP). This finding suggests that an axisymmetric model, such as that used by Gray [13, 14], is not adequate for modeling the BLI characteristics for the STARC-ABL.

Establishing a set of guidelines defining which geometry OML features for CFD analysis need to be considered in conceptual design, and which can be tailored later in preliminary design, is helpful. These guidelines will enable CFD usage for modeling BLI physics at a stage where design knowledge is limited and high dimensionality adds additional degrees of freedom which cannot be tractably addressed in conceptual design. This paper aims to provide some insight on this aspect, through a systematic set of experiments, which identify the sensitivity of the ingested boundary layer effects to the airframe design. The scope is restricted to tube and wing type BLI concepts. This work is a continuation of a previous study that focused on the conceptual design of a fuselage trailing edge mounted BLI propulsor [15]. This previous work also showed the sensitivity of the BLI effects to the propulsor size and throttle setting. The present work forms a core component of a coupled aero-propulsive conceptual design methodology for BLI aircraft, currently under development by the author.

The rest of the paper is organized as follows: Sec. III formulates the overarching research problem for this paper, followed by a description of the theory used to define the BLI effects in Sec. IV. Sec. IV also outlines the experimental objectives and supporting material needed for the experiments. Sec. V provides details on each experiment conducted, presents the results, and comments on the findings. Sec. VI summarizes the key takeaways from this paper.

III. Research Formulation

The airframe geometry OML can be roughly defined by two types of parameters: macro and detailed. At the most general level, macro parameters are lengths, areas, angles, i.e., quantities that one typically associates with *sizing* an airframe (or engine). Detailed parameters on the other hand define geometry features like curvature radii, airfoil camber, etc. These are finer features of the geometry that add definition to the airframe shape. Fig. 1 shows examples of a few macro and detailed parameters. With regards to modeling BLI effects, macro and detailed features that have the strongest impact on the BLI effects can be called active variables, while those that have a relatively smaller impact, and can thus be set to fixed values, can be called inactive variables.


Fig. 1   Examples of airframe macro and detailed variables

In idealized 3D boundary layer theory, at any given point there is a zone of influence and a zone of dependence that can be identified from examining the characteristics and sub-characteristics of the governing equations [16] as shown in Fig. 2. As explained by McLean [17], for a column normal to the surface through a given point P, the extents of these zones are defined by the "widest range of streamline directions passing through the column"[17]. Thus, the flow at every point in this column is dependent on properties of the streamlines contained within the zone of dependence, while the flow properties along the column at P affect the streamlines contained in the zone of influence. McLean also highlights the finite influence of upstream perturbations on the downstream boundary layer flow by comparing two flows, with one subjected to a small patch of surface roughness. McLean states that "when a boundary-layer flow is perturbed in some way, it remembers the perturbation and then gradually forgets" [17]. In other words, impact of small upstream perturbations in the zone of dependence decays after a finite distance.

In idealized theory, there is no influence or dependence of the flow outside these zones on the flow properties along the column at P. Flow in the zone of influence can only have an indirect upstream impact if the flow affects the externally imposed pressure gradient. If the change is small, such as that introduced by a small bump on the surface in the zone of influence, then as McLean claims, the direct upstream influence is limited to a small distance. If however there is flow separation as a result of this disturbance, the upstream influence is more significant. Lastly, McLean explains that for real flows where the effect of lateral viscous diffusion is present, the effects of flow outside the idealized zones are only significant over distances on the order of the boundary layer thickness. The discussion above implies that viscous effects are more localized than pressure effects. The latter are predominantly driven by the inviscid flow field variations, determined by the shape of the entire airframe, while the former are more strongly influenced by the geometry that fall within the zone of dependence of the boundary layer. When considering the impact of airframe geometry on the ingested boundary layer properties, where the boundary layer is being ingested is critical. This is determined by the position of the engine, specifically, the circumferential (θ) and axial location (Δx) on the airframe as shown in Fig. 1.

Kenway and Kiris [12] found sensitivity of the distortion pattern at the STARC-ABL BLI propulsor AIP to the wing downwash, verified by Gray [18], who also found the vertical tail to have an impact. The streamtube ingested by a fuselage trailing edge propulsor has a larger zone of dependence than for propulsors that are mounted on the fuselage, like on the D8 or NOVA-BLI. The active variable spaces for the D8 and NOVA-BLI are likely to be dissimilar, given the different circumferential positions of the engines. The axial location of the engine has two contributions. The first relates to the mass, momentum, and energy defect growth in the boundary layer, proportional to the length of the surface over which the boundary layer grows. The second has to do with the impact of small perturbations on the flow. Small perturbations in the zone of dependence have more time to die out
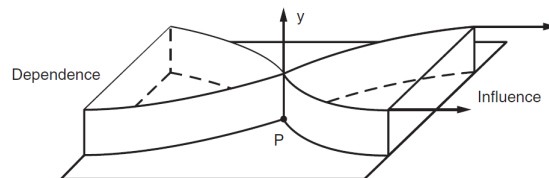
Fig. 2   Zones of influence and dependence in 3D boundary layers (reproduced from [17])

before they reach the engine in instances where the distance between the engine and perturbation is long enough. This distance, thus, also affects which upstream geometry parameters affect the ingested boundary layer. Lastly, all geometry features that fall in the zone of influence, rather than in the zone of dependence, are unlikely to have impacts on the upstream properties, as discussed before. This statement is expected to be valid as long as there is no excessive flow separation or shocks, i.e., no major adverse pressure gradient effects, which is also a criterion for separating small and large perturbations. From this discussion, a general hypothesis is formed to answer the research question posed in Sec. II, as follows: *parameters present in the active and inactive variable spaces are determined by the axial and circumferential location of the engine on the airframe. The axial location defines the distance over which the boundary layer grows, as well as the impact of small perturbations in the zone of dependence. The circumferential location determines how much the wing contributes to the ingested boundary layer properties. Within the active space, if perturbations in detailed parameters do not result in shocks or flow separation in the ingested streamtube, then these parameters can be defaulted for conceptual design purposes since the BLI effects in this instance are more sensitive to changes in macro parameters.* Thus, the objective of this study is to determine which airframe design parameters fall under the active and inactive spaces, while quantifying the relative sensitivity of the BLI effects to the macro and detailed variables.

IV. Methodology

A. Airframe Performance Bookkeeping

The portion of the airframe wake that would have contributed to the aircraft drag for a non-BLI aircraft is partially ingested by the propulsor for BLI concepts. Thus, the ingested boundary layer contributes to both thrust and drag, and separating these components is ambiguous. Recognizing deficiencies of the thrust-drag bookkeeping approach for highly integrated aircraft concepts, alternative bookkeeping approaches have been proposed in literature. One such approach is the power balance formulation proposed by Drela [19] and extended by Sato [20] and Hall [21]. This approach involves a mechanical energy balance, as opposed to the traditional momentum balance. Another bookkeeping approach involves an exergy analysis, developed by Arntz [22], which takes into account both aircraft thermal and mechanical energy. This method is more global than the power balance approach. Since aircraft thermal analysis is not considered in this paper, the power balance bookkeeping approach is adequate, and as will be shown later, can be easily adapted to work with tools that rely on thrust-drag bookkeeping.

B. Power Balance Formulation

The control volume used for developing the power balance approach can be seen in Fig. 3 (inspired by [21]). Though the vehicle shown is similar to a notional D8, the methodology is valid for all BLI concepts considered in this paper. The control volume is cylindrical with the upstream and downstream (Trefftz Plane - S_{TP}) boundaries normal to the freestream flow, and the side boundaries parallel to the freestream. The side boundaries are assumed to be sufficiently far from the body and thus flow there is at ambient conditions. An infinitesimal cut in the control volume links the outer boundary, S_O, with the inner boundary, S_B, which wraps over the surface of the body and around the propulsor inlet and exit planes, shown in red in the figure. While the propulsor itself is not part of the control volume, the planes at stations
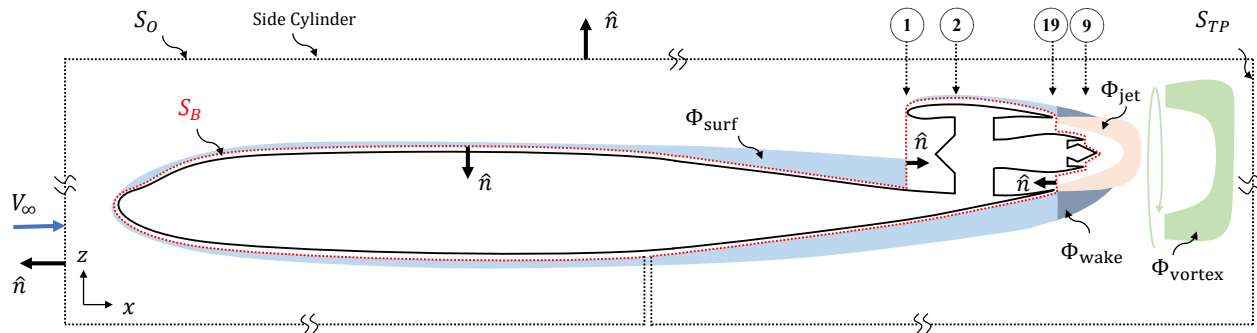

Fig. 3   Control volume for power balance based BLI analysis

1, 19, (and 9 for BLI propulsors with a core) represent boundaries where flow exits and enters the control volume. S_B is represented by an inward pointing normal $\hat{\mathbf{n}}$, which is outward pointing for S_O.

The power balance equation can be expressed for a control volume with the boundary S_O far away from the body surface S_B as follows [21]:

$$P_{K_{out}} - \Phi_{jet} = \Phi_{surf} + \Phi_{wake} + \Phi_{vortex} + \Phi_{shock} - F_X V_\infty - P_{K_{in}} \tag{1}$$

where P_K is the net mechanical power added to the flow by the propulsor across the surface S_B. This term represents the net pressure-work and kinetic energy flux rate, and captures the contributions from turbomachinery and combustors not included in the control volume boundary S_B. This quantity is calculated as follows

$$P_K = \oiint -\left[(p - p_\infty) + \frac{1}{2}\rho\left(V^2 - V_\infty^2\right)\right] \mathbf{V} \cdot \hat{\mathbf{n}} dS_B \tag{2}$$

where $V^2 = \mathbf{V} \cdot \mathbf{V}$ is the square of the magnitude of the local velocity vector $\mathbf{V}$, p is the static pressure, and ρ is the static density, at a given location. Freestream quantities are denoted by $(\cdot)_\infty$. Since the flow is tangent to the control volume boundary S_B everywhere over the airframe except the propulsor inlet and outlet planes i.e., stations 1, 19 and 9 in Fig. 3, the contributions to P_K from these surfaces is zero since $\mathbf{V} \cdot \hat{\mathbf{n}} = 0$. Therefore, P_K can be expressed as follows:

$$P_K = P_{K_{in}} + P_{K_{out}} \tag{3}$$

where $P_{K_{in}}$ and $P_{K_{out}}$ are the non-zero P_K contributions evaluated at the propulsor inlet and exit areas (station 19 for a ducted fan, and both 19 and 9 for a BLI turbofan) respectively. Since the state of the flow exiting the propulsor can be estimated in conceptual design using a 1D thermodynamic cycle analysis tool, which assumes uniform axial flow, $P_{K_{out}}$ for a turbofan can thus be calculated rather easily as follows

$$\begin{aligned} P_{K_{out}} &= \left[(p_{19} - p_\infty) + \frac{1}{2}\rho_{19}\left(V_{19}^2 - V_\infty^2\right)\right] V_{19} A_{19} \\ &+ \left[(p_9 - p_\infty) + \frac{1}{2}\rho_9\left(V_9^2 - V_\infty^2\right)\right] V_9 A_9 \end{aligned} \tag{4}$$

Recognizing that the flow rate $\dot{m} = \rho A V$, for a given flow area A, one obtains

$$\begin{aligned} P_{K_{out}} &= (p_{19} - p_\infty) V_{19} A_{19} + \frac{1}{2}\dot{m}_{19}\left(V_{19}^2 - V_\infty^2\right) \\ &+ (p_9 - p_\infty) V_9 A_9 + \frac{1}{2}\dot{m}_9\left(V_9^2 - V_\infty^2\right) \end{aligned} \tag{5}$$

Note that the flow exiting the propulsor is in a direction opposite to the unit normal vector at that plane, which cancels the negative sign outside the integrand in Eq. (2). Significant variations in the thermodynamic properties in the ingested boundary layer invalidate the uniform flow assumption, and thus the integral equation must be used to calculate $P_{K_{in}}$ from CFD as shown

$$P_{K_{in}} = \iint -\left[(p_1 - p_\infty) + \frac{1}{2}\rho_1\left(V_1^2 - V_\infty^2\right)\right] \mathbf{V_1} \cdot \hat{\mathbf{n}} dS_1 \tag{6}$$

This term is related to the thermodynamic properties of the ingested boundary layer and is a measure of the ingested profile drag power [23]. It is thus directly dependent on the airframe geometry and indirectly on the propulsor through fan size and throttle setting. In the case of a podded propulsor, $V_1 = V_\infty$ and $p_1 = p_\infty$ for an isentropic streamtube and hence $P_{K_{in}} = 0$ for the non-BLI case. On the other hand, $P_{K_{out}}$ is dependent on the propulsor jet exhaust velocities, pressures, and densities, which are dependent on the shaft power, component efficiencies, and thermal efficiency, and can thus be mapped to the engine fuel burn. $P_{K_{out}}$ is indirectly dependent on the airframe geometry through the propulsive power requirements set by the airframe.

The viscous dissipation inside the control volume, represented by Φ, accounts for the conversion of flow kinetic energy to thermal energy. Dissipation in the control volume occurs predominantly in the boundary layers on the airframe surface, followed by the propulsor jet, wake, trailing vortex sheet, and in any shocks on the body. Thus, the total dissipation Φ can be decomposed into distinct contributions as shown by

$$\Phi = \underbrace{\Phi_{surf} + \Phi_{wake} + \Phi_{vortex} + \Phi_{shock}}_{\Phi_{afm}} + \Phi_{jet} \tag{7}$$

5

where Φ_{afm} denotes the dissipation contributions from the airframe and Φ_{jet} represents the jet mixing dissipation from the propulsor exhaust. The latter is equal to the excess mechanical energy deposition rate at the propulsor outlet [21] and can be calculated at the propulsor outlet area, assuming perturbation velocities $v = w = 0$, as follows:

$$\Phi_{jet} = \iint \left[\frac{1}{2} \rho \, (V - V_\infty)^2 \, V + (p - p_\infty)(V - V_\infty) \right] dS_{PO} \tag{8}$$

where S_{PO} is the propulsor outlet area. For the control volume shown in Fig. 3, Eq. (8) is evaluated over the core and bypass nozzle exit areas, i.e., at stations 9 and 19 respectively, and then summed. If in addition to the 1D flow assumption, one assumes no variations in the axial flow over the propulsor exit areas, then Φ_{jet} can be calculated using a cycle analysis tool, like in the case of $P_{K_{out}}$, as follows:

$$\begin{aligned} \Phi_{jet} = {} & (p_{19} - p_\infty)(V_{19} - V_\infty) A_{19} + \frac{1}{2} \dot{m}_{19} (V_{19} - V_\infty)^2 \\ & + (p_9 - p_\infty)(V_9 - V_\infty) A_9 + \frac{1}{2} \dot{m}_9 (V_9 - V_\infty)^2 \end{aligned} \tag{9}$$

Eq. (1) is the power balance formulation for a BLI configuration. For a non-BLI configuration, since $P_{K_{in}}$ is zero, Eq. (1) can be written for the non-BLI * case as

$$P'_{K_{out}} - \Phi'_{jet} = \Phi'_{surf} + \Phi'_{wake} + \Phi'_{vortex} + \Phi'_{shock} - F'_X V_\infty \tag{10}$$

Eqs. (1) and (10) are written in a manner where terms in the power balance equation that depend only on the propulsor exhaust jet are expressed on the left-hand side, while terms related to the airframe and ingested boundary layer are expressed on the right-hand side. Thus, the left-hand side terms can be calculated from a simple 1D engine cycle model with uniform flow assumptions, while the right-hand side terms can be obtained from the aerodynamics model. The right-hand side terms can be thought of as a requirement for the propulsion model, analogous to the situation where airframe drag is a thrust requirement for a non-BLI propulsor.

C. Relating Power Balance to Thrust and Drag

For a net axial force requirement, i.e., where $F_X = F'_X = \mathcal{F}_X$, the propulsor requirement in Eq. (1) for the BLI configuration can be expressed in terms of dissipation components in the non-BLI case and changes in dissipation that occur as a result of the engines ingesting the boundary layer, as

$$\begin{aligned} P_{K_{out}} - \Phi_{jet} = {} & \Phi'_{surf} + \Phi'_{wake} + \Phi'_{vortex} + \Phi'_{shock} - \mathcal{F}_X V_\infty \\ & - (P_{K_{in}} + \Delta\Phi_{surf} + \Delta\Phi_{wake} + \Delta\Phi_{vortex} + \Delta\Phi_{shock}) \end{aligned} \tag{11}$$

where the Δ terms in the above expression are defined by

$$\Delta\Phi_{component} = \Phi'_{component} - \Phi_{component} \tag{12}$$

The main challenge with adopting power balance in conceptual design is that current industry standard engine and airframe sizing tools like NPSS and FLOPS function in the thrust-drag bookkeeping domain. It is possible however to translate power balance into an equivalent thrust-drag formulation, under certain reasonable assumptions, which can then be used with existing tools. Consider the power balance expression for a non-BLI configuration as shown in Eq. (10). Using the definitions for $P_{K_{out}}$ and Φ_{jet} in Eqs. 5 and 9 respectively, one can see that $P'_{K_{out}} - \Phi'_{jet}$ evaluates to

$$\begin{aligned} P'_{K_{out}} - \Phi'_{jet} = {} & [\dot{m}_{19} V_{19} + \dot{m}_9 V_9 - (\dot{m}_{19} + \dot{m}_9) V_\infty] V_\infty \\ & + [(p_{19} - p_\infty) A_{19} + (p_9 - p_\infty) A_9] V_\infty \end{aligned} \tag{13}$$

Assuming $\dot{m}_{19} + \dot{m}_9 = \dot{m}_1$, it can clearly be seen that the above expression is equal to $F'_N V_\infty$, where F'_N is the net thrust (gross thrust minus *freestream* ram drag) for a separate flow turbofan engine without BLI. The assumption of mass continuity above ignores contributions from fuel flow and customer bleed extractions on the propulsor exit mass flow. These contributions are however usually small, compared to the total flow rate, and thus it is acceptable to neglect them

---

*To be consistent with literature, the notation $(\cdot)'$ is used to represent quantities that are obtained with reference to non-BLI configurations, while un-primed terms represent quantities calculated for the BLI case.

in early conceptual design. Eq. (13) can also be used for a ducted fan, like that on a STARC-ABL, by ignoring terms related to the core (9). In this situation, since there is no bleed or fuel flow, the mass continuity assumption above is exactly valid. It should be emphasized that while the expression for $P_{K_{out}} - \Phi_{jet}$ is identical for BLI and non-BLI cases, labeling it as net thrust times freestream velocity is only appropriate for non-BLI aircraft since the notion of thrust and drag for BLI aircraft is ambiguous as discussed before. Using the above observation and dividing each term in Eq. (10) by V_∞, one sees that Eq. (10) can now be written as

$$F'_N - \left(\frac{\Phi'_{surf} + \Phi'_{wake} + \Phi'_{vortex} + \Phi'_{shock}}{V_\infty} \right) = -F'_X \tag{14}$$

For the podded case, $F'_X = D' - F'_N$. Therefore, it must follow that

$$\Phi'_{surf} + \Phi'_{wake} + \Phi'_{vortex} + \Phi'_{shock} = \Phi'_{afm} = D'V_\infty \tag{15}$$

Finally, one can express the power balance formulation for a BLI vehicle by substituting Eq. (15) in Eq. (11) to obtain

$$\underbrace{P_{K_{out}} - \Phi_{jet}}_{\approx F'_N V_\infty} = D'V_\infty - \underbrace{F_X V_\infty}_{P_{ex}} - \underbrace{\beta}_{\approx \Delta D' V_\infty} \tag{16}$$

where P_{ex} is the excess power requirement and $\beta \equiv P_{K_{in}} + \Delta\Phi_{surf} + \Delta\Phi_{wake} + \Delta\Phi_{vortex} + \Delta\Phi_{shock}$. Eq. (16) expresses the power balance in terms of quantities that are well defined and understood for non-BLI vehicles (net thrust, drag, and excess power requirements) and identifies the additional elements needed to account for the BLI impacts, thus sidestepping the thrust-drag ambiguity issue with BLI aircraft. The terms represented by β are the BLI effects. These terms capture the changes to the propulsive power requirements as a result of placing the engines in a manner that results in the partial or complete ingestion of the airframe boundary layer. By definition, these are zero for a non-BLI aircraft.

D. BLI Effects

The analysis in the preceding subsection identified certain terms that are related only to BLI. Calculating these terms allows one to determine the impact of BLI on the vehicle design and performance.

$\Delta\Phi_{surf}$ This term represents the change in total surface dissipation of the airframe as a result of placing the propulsors in the boundary layer flow. Sato [20] and Hall [21] showed that surface dissipation for a body is relatively insensitive to pressure changes due to throttle effects. Therefore, this term quantifies the impact of configuration wetted area changes between a podded engine airframe and the BLI variant.

$\Delta\Phi_{vortex}$ This term represents the change in dissipation of the trailing vortex system for the wing far downstream of the body. The lift distribution of the wing and hence the trailing vortices is affected by the propulsor placement. Configurations where the nacelles are placed over the wing are likely to have a stronger impact than in cases where the engines are fuselage mounted and far from the wing. However, the impact of the engine placement on the vortex dissipation will have similar contributions for both the BLI and non-BLI cases, and thus this term can be neglected.

$\Delta\Phi_{shock}$ This term represents the change in the dissipation as result of changes to the shock strengths on the airframe, going from the non-BLI to BLI configurations. A well designed transonic airplane will minimize interference effects and adverse contributions from shocks, whether it is a podded or a BLI configuration. Even if shocks are present, it can be assumed that the contributions for the BLI and non-BLI cases are similar, and thus the difference is negligible.

$\Delta\Phi_{wake}$ The change in wake dissipation is a function of the amount of boundary layer ingested. Hall [23] suggests that a good approximation for estimating this change in is to use the following equation:

$$\dot{E} = \iint \left[\frac{1}{2}\rho \left(u^2 + v^2 + w^2 \right) (V_\infty + u) + (p - p_\infty) u \right] dS_{PO} \tag{17}$$

  evaluated at the nozzle outlet plane for an un-powered configuration. In other words, the reduction in wake dissipation can be approximated as the reduction in amount of mechanical flow energy being deposited off the airframe.

$P_{K_{in}}$ This term captures the mechanical energy defect of the ingested boundary layer flow, which affects the propulsive power requirements. This term can be calculated from Eq. (6) as described before.

7

η_{PR} The pressure recovery seen by the engine is another factor that shows appreciable differences between BLI and non-BLI engines, even though it does not explicitly feature in the power balance equation. For non-BLI configurations, the biggest source of pressure loss in the flow ingested by the propulsor is due to the inlet. Typically, the pressure recovery, η'_{PR}, for non-BLI propulsors is defined as:
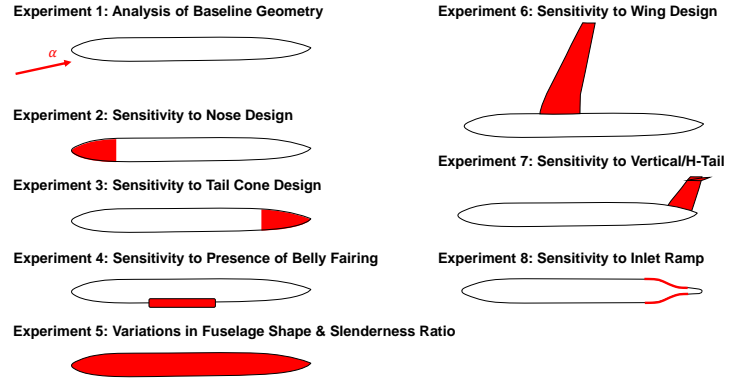
$$\eta'_{PR} = \frac{p_{t_2}}{p_{t_1}} \tag{18}$$

with the assumption that $p_{t_1} = p_{t_0}$. However, for BLI configurations, there are additional losses in the ingested boundary layer flow that are a function of the airframe geometry. Thus for BLI configurations, it is more appropriate to define the pressure recovery as:

$$\eta_{PR} = \frac{p_{t_2}}{p_{t_1}} \frac{p_{t_1}}{p_{t_0}} = \frac{p_{t_2}}{p_{t_0}} \tag{19}$$

E. Overview of Sensitivity Studies

Having described the main BLI effects, it is now possible to present an overview of the experiments that are run. Regions of the airframe considered in this study are shown in Fig. 4. Details on the approach for each experiment are presented in the following section along with the results. A systematic experimental approach is designed to maximize the information gained from a small set of trials. This endeavor is constrained to tube and wing BLI aircraft, predominantly in 150-180 passenger class. The results provide a physics based insight into the relation between engine position and the sensitivity of BLI effects at this location to a limited

Fig. 4   Overview of experiments to evaluate BLI effects sensitivities

set of airframe design features. The active and inactive variable spaces, within this design scope, are thus identified. Rule of thumb guidelines for defaulting geometry detail, when generating surrogates of the BLI effects in concept design, are obtained. These suggestions are based on the relative sensitivity of the BLI effects to the macro and detailed parameters, gleaned from the experimental results. All cases are run at $M_\infty = 0.8$, at an altitude of 35,000ft, which is a typical cruise flight condition. Standard atmosphere properties are assumed. The commercially available CFD tool STAR-CCM+, by Siemens, is used for the aerodynamics analysis. Geometry generation and modification capability is provided by OpenVSP, SolidWorks, and STAR-CCM+ CAD tools.

F. Baseline Airframe Geometry

A schematic of the baseline geometry and experimental setup in CFD is shown in Fig. 5. The baseline geometry consists of an axisymmetric fuselage only, with a cylindrical center-body, an elliptical nose, and a conical aft section. This simplified representation of the aircraft enables a ground-up approach to assess the sensitivities, gradually building up to more complex geometry over the course of the experiments. As a result, key features that influence the BLI effects can be identified more easily than in the case where a complex geometry is used as a starting point and then parameterized. The transition between the nose and center-body, and center-body and tail is smooth and gradual to avoid shocks and flow separation at high Mach numbers. Subsequent modifications to the geometry that may produce shocks or separation can thus be assessed against a relatively ideal baseline. The length of the fuselage is 39.12m. This length is similar to the Boeing 737-8 [24] and is thus also comparable to the NOVA-BLI, D8, and STARC-ABL concepts that have been sized for 150-180 passengers. The diameter of the baseline center-body is 3.89m, defined such that the area of the cylindrical center-body cross section matches the area of the elliptical Boeing 737-8 center-body cross section [24]. The baseline features a blunt trailing edge with an arbitrarily set radius of 0.15m to avoid meshing issues around a sharp point trailing edge.
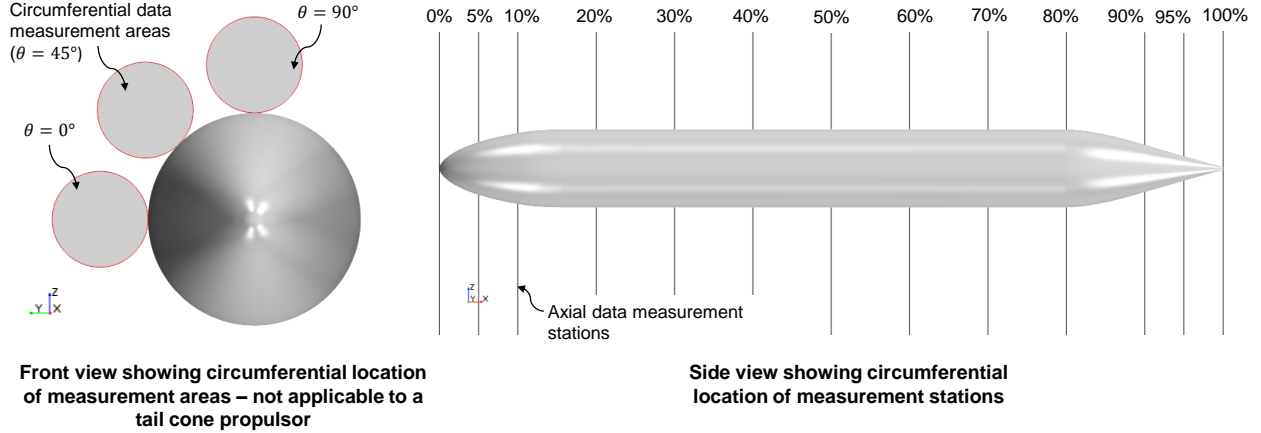
Fig. 5 Schematic showing baseline geometry and measurement stations for the experiments.

Along the axial direction, a series of planes are defined on which surface integrals for non-dimensional BLI effects $C_{P_{K_{in}}}$, $C_{\dot{E}}$, and η_{PR} are calculated on pre-defined circular areas, shown with red outlines in Fig. 5. Non-dimensionalization of the BLI effects is done by dividing the dimensional quantities by $\frac{1}{2}\rho_\infty V_\infty^3 S_{ref}$, where S_{ref} is a reference area, set to 1 for the experiments. These integration areas represent a fictitious propulsor inlet and outlet at different circumferential locations. At each axial plane, except at the trailing edge, these integration areas are tangent to the fuselage surface, and are located at 0°, 45°, and 90° relative to a coordinate system whose origin coincides with the centroid of the cross sectional area at a given axial location. Defining the measurement locations in such a fashion allows for the experiments to establish a relation between engine axial and circumferential location on the fuselage, and the sets of active and inactive design variables. The axial station at the nose is shown in Fig. 5 for completeness, but no quantities are calculated at this station. For the axial station at the trailing edge, the center of the integration area is coincident with the centroid of the trailing edge, thus representing a fictitious tail cone propulsor like on the STARC-ABL. The diameter of these integration areas is defined as 1.75m, which is approximately the fan diameter of the LEAP-1B engines on the Boeing 737-8 [25]. This diameter is fixed for all experiments.

G. Comments on CFD Model Setup

All CFD runs leverage STAR-CCM+ built-in capability for surface and volume mesh generation. An unstructured Cartesian mesh is used, with prism layers for near wall refinement to capture the boundary layer. The near wall spacing is calculated such that a wall $y^+ \leq 1$ is achieved over the entire surface. A mesh and CFL sensitivity study is conducted to pick the optimal settings to balance accuracy, robustness, and solver convergence time. The baseline fuselage is used as the geometry. The mesh quality is evaluated on the following criteria:

1) Sensitivity of the BLI effects to the mesh settings, specifically mesh size
2) Whether axisymmetric flow is captured. An axisymmetric fuselage at zero incidence to the flow and no side-slip should theoretically have axisymmetric flow. A half domain 3D solution should reflect this property.
3) Solver convergence - determined by looking at residual history and convergence plots of BLI quantities at different locations on the fuselage.

To save time and computational resources, the same mesh settings are used over the course of all the fuselage only experiments. For trials where the wing or empennage are added to the geometry, the mesh settings for the fuselage are kept the same as the baseline. The surface mesh settings for the additional component are assessed over two to three trials. From the CFL study, a value of 20 is chosen for all cases without a wing, and 10 for trials with a wing. These values ensure quick and reliable solver convergence. All results are obtained under the assumption of steady state conditions, by solving the Reynolds Averaged Navier Stokes equations. The solver uses an implicit time integration scheme with second order upwind spatial discretization. The AUSM+ FVS [26] scheme is used with the Venkatakrishnan limiter for evaluating the inviscid fluxes. Fully turbulent conditions are assumed, and the SST k-ω turbulence model [27] is chosen. A spherical freestream boundary with a radius approximately 30 times the fuselage length is defined, and x-z plane symmetry in all cases allows for half the domain to be modeled.

9

H. Significant Difference Criterion

Sensitivity of the BLI effects to the geometry is determined by comparing the numerical results from the modified geometry to the established baseline. To assess whether these differences are significant, some sort of threshold must be established. Since the primary objective of BLI is to minimize fuel burn, a simple condition for identifying significant changes can be obtained by comparing differences in fuel flow rate at a single operating point due to changes in thrust required and inlet pressure recovery.
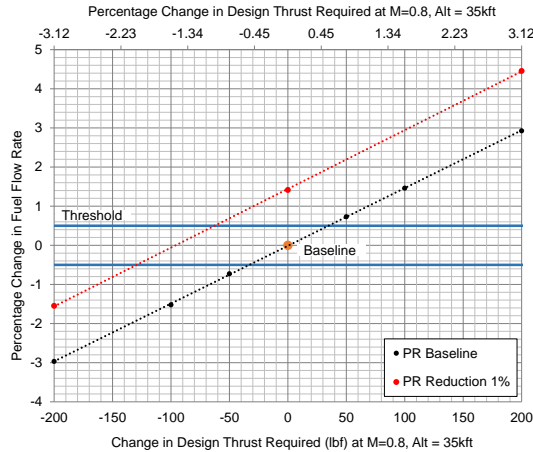
Fig. 6 Variation of fuel flow rate as a function of change in design thrust required and inlet pressure recovery for an engine on a generic 150-pax aircraft

A notional engine for a generic 150-pax vehicle (similar to the LEAP-1B for the 737-8) is modeled in the Environmental Design Space [28] framework using a Multi-Design Point approach [29], with five design points: Sea Level Static (SLS), takeoff (TKO), hot day takeoff, Top of Climb (TOC), and Aerodynamic Design Point (ADP). The TOC and ADP points are at $M_\infty = 0.8$ at 35,000 ft. As shown in Fig. 6, the baseline cruise fuel flow rate is shown with an orange marker. Subsequently, the design thrust requirement at TOC is varied between ±200 lbf (±3.12%) relative to the baseline and the corresponding percent change in fuel flow rate is tracked, shown with black markers in Fig. 6. To avoid lapse rate effects, the ratio of TOC/SLS and TOC/TKO thrust requirement is kept the same for each case regardless of the TOC thrust value. A similar exercise is conducted for the situation where the inlet pressure recovery is reduced by 1% relative to the baseline, shown with red markers.

The blue lines correspond to a ±0.5% change in fuel flow rate relative to the baseline, and are defined as critical thresholds beyond which this change is significant. These thresholds map to a 35 lbf change in thrust required (0.55% of baseline TOC thrust requirements) and a 0.35% change in pressure recovery. It is important to note that the objective of the experiments is not so much to quantify the BLI benefit, but rather, quantify the *difference in the estimate for the BLI effects* due to changes in airframe design. As such, the *change* in the estimate for the BLI effects between two trials, translated to an equivalent change in force for $C_{P_{K_{in}}}$ and $C_{\dot{E}}$, is compared against the threshold values derived above. For η_{PR}, the percentage difference between two cases is compared to the threshold value of ±0.35%.

V. Experiments: Approach, Results, and Discussion

A. Experiment 1: Analysis of Baseline Geometry

The objective of this experiment is to analyze the baseline geometry at two angles of attack. Cases 1.1 ($\alpha = 0°$) and 1.2 ($\alpha = 2°$) are typical cruise flight conditions. For this reason, these cases are defined as baselines. Results from other experiments are compared to the reference case results from 1.1 or 1.2, depending on the angle of attack, unless otherwise specified. Fig. 7 compares the axial and circumferential trends in BLI effects for cases 1.1 and 1.2. Red, blue, and green colored markers are used to denote quantities at the 0°, 45°, and 90° circumferential stations respectively.

1. Trends for $C_{P_{K_{in}}}$ and η_{PR}

Positive values of $C_{P_{K_{in}}}$ at all stations imply reductions in propulsive power requirements relative to the non-BLI case, with the greatest propulsive benefit achieved at the 100% axial station (A1.00) propulsor. However, this benefit is somewhat offset by a considerable drop in η_{PR}. The trends for $C_{P_{K_{in}}}$ and η_{PR} with axial location are opposite to each other, evident in Fig. 7. The counteracting trends of $C_{P_{K_{in}}}$ and η_{PR} with axial distance highlight a challenge in designing BLI vehicles. To maximize the lower inflow momentum benefit (higher $C_{P_{K_{in}}}$), a thicker boundary layer is desired. However, a thicker ingested viscous layer comes at the cost of low pressure recovery and high distortion, which penalizes engine performance. A feasible design must have a favorable net impact.

The trends for $C_{P_{K_{in}}}$ can be better understood by looking at the two contributing sources, i.e., the boundary layer energy thickness and the flow pressure. First, Eq. (6) is divided by $q_\infty V_\infty S_{\text{ref}}$ to non-dimensionalize $P_{K_{in}}$. Then, upon
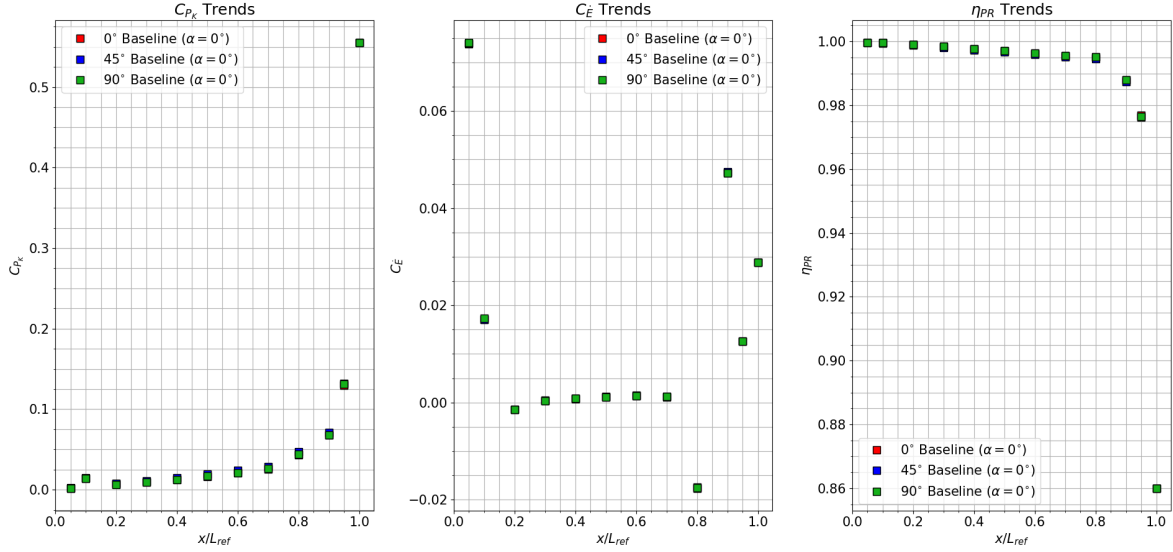
(a) Case 1.1: $\alpha = 0°$
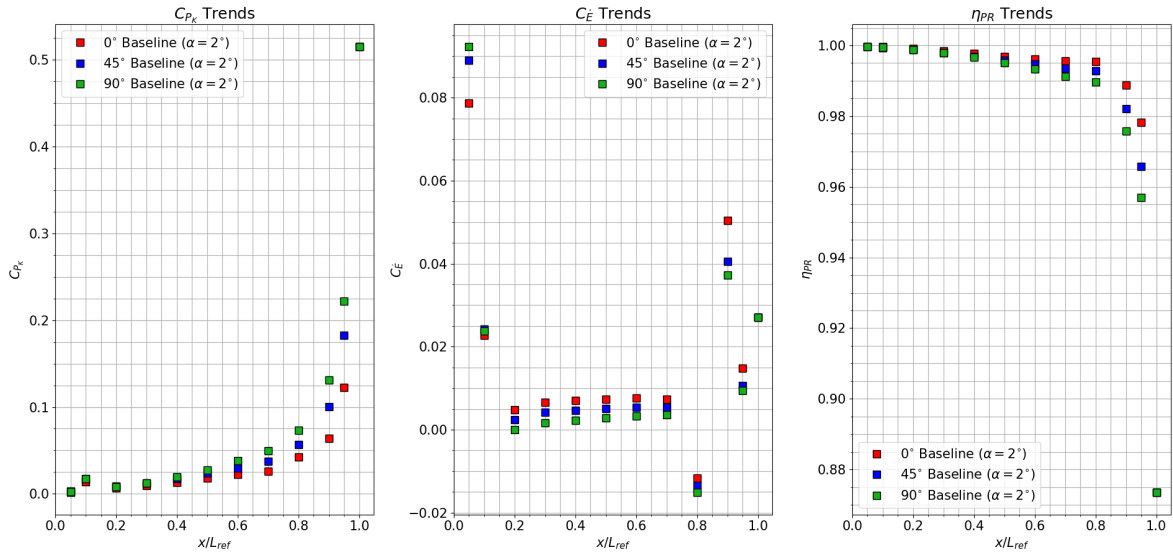
(b) Case 1.2: $\alpha = 2°$
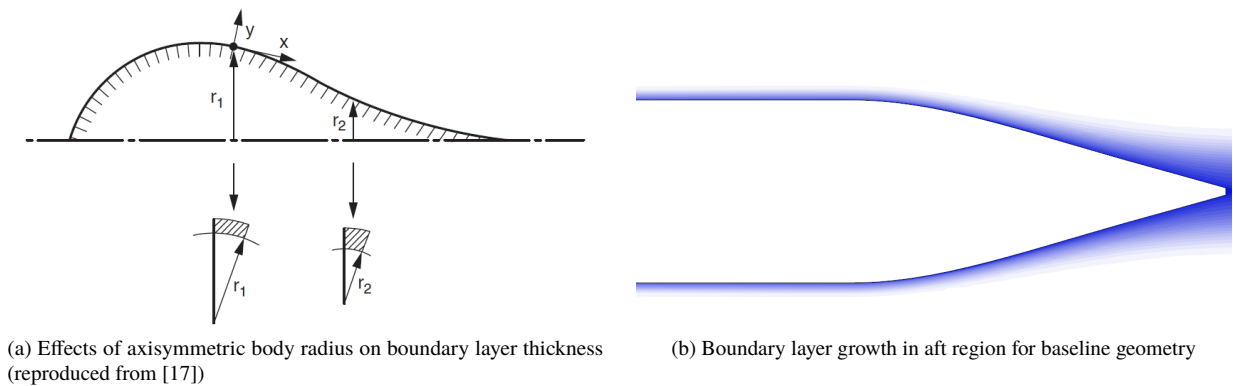
Fig. 7 Experiment 1: axial and circumferential trends in BLI effects for the baseline geometry

rearranging terms, an expression for $C_{P_{K_{\text{in}}}}$ at a given measurement station i is obtained as follows:

$$C_{P_{K_{\text{in}}}} = \iint \left[\frac{\rho_i V_i}{\rho_\infty V_\infty} \left(1 - \frac{V_i^2}{V_\infty^2} \right) - C_{p_i} \frac{V_i}{V_\infty} \right] \frac{dS_i}{S_{\text{ref}}} \tag{20}$$

Here, $C_{p_i} = \frac{p_i - p_\infty}{\frac{1}{2}\rho_\infty V_\infty^2}$ is the pressure coefficient and V_i is the axial velocity magnitude at a given station. The first term in Eq. (20) is like an ingested kinetic energy thickness. The second term captures the direct contribution of the inviscid flow pressure at a given axial location on $C_{P_{K_{\text{in}}}}$. The indirect contribution of the pressure field arises through the impacts of the pressure gradient on the ingested boundary layer energy defect. Unlike $C_{P_{K_{\text{in}}}}$, pressure recovery is less strongly dependent on the inviscid flow pressure. The influence of pressure is only indirect, through the effects of the pressure gradient on the boundary layer thickness, as long as there are no shocks or flow separation. The relatively gradual

11

change in both $C_{P_{K_{in}}}$ and η_{PR} up to 80% of the fuselage length can be attributed to boundary layer growth along axial distance, where the boundary layer thickness, $\delta \propto x^{0.8}$, from simple turbulent flat plate boundary layer relations. As the boundary layer grows, the increasing viscous losses manifest as lower averaged total pressure at the integration planes normal to the boundary layer, which results in a drop in η_{PR} with axial location. However, the thickening boundary layer also presents a larger kinetic energy defect, which translates to an increase in $C_{P_{K_{in}}}$ with axial distance. The rapid change at the aft end is driven by the tapering of the fuselage and the adverse pressure gradient effects on the boundary layer. According to McLean, the variation in body radius, from the symmetry axis, affects stretching of the boundary layer circumferentially, as illustrated in Fig. 8a. In this figure, the side cross sectional view is shown on top, while the illustrations below show the front cross sectional view and the circumferential stretching of the boundary layer. A smaller radius, i.e., in the tapering region of the fuselage, (indicated by r_2 in Fig. 8a) increases the boundary layer growth rate relative to a planar flow with the same pressure gradient [17]. The taper, in conjunction with the adverse pressure gradient, contributes to the thicker boundary layer seen in Fig. 8b for the baseline geometry aft region. The A1.00 plane shows the largest $C_{P_{K_{in}}}$ and the smallest η_{PR} since this location ingests the entire circumferential extent of the boundary layer, unlike the upstream stations that only ingest a sliver.

(a) Effects of axisymmetric body radius on boundary layer thickness (reproduced from [17])

(b) Boundary layer growth in aft region for baseline geometry

**Fig. 8   Effects of axisymmetric body radius on boundary layer growth**

2. Trends for $C_{\dot{E}}$

The change in wake dissipation, $C_{\dot{E}}$, is comprised of two contributing sources. The first, $\frac{1}{2}\rho \left(u^2 + v^2 + w^2 \right) \left(V_\infty + u \right)$, is like a perturbation kinetic energy rate term, quantifying the dissipation contributions due to non-uniformity in the flow velocity. Any significant differences with respect to freestream flow will result in mixing losses, and thus, this term is positive, or zero in situations where the flow is at freestream conditions. In regions of reversed flow, this term is negative. The other term, $(p - p_\infty) u$, is the pressure defect work rate due to pressure differences in the flow relative to freestream [19]. This term is usually negative since $p < p_\infty$ typically implies $u > 0$ since $V > V_\infty$, while $p > p_\infty$ suggests $u < 0$. In situations where the pressure coefficient is large and negative (e.g. at the 80% axial station) the pressure work term dominates and the net result is a negative value for $C_{\dot{E}}$, as seen in Fig. 7. Positive values for $C_{\dot{E}}$ imply a net reduction in propulsive power requirements for the BLI case, relative to the non-BLI aircraft. Negative values on the other hand suggest a detrimental effect, or an increase in the propulsive power requirements for the BLI case. Like $C_{P_{K_{in}}}$, $C_{\dot{E}}$ also shows both a direct and indirect dependence on the pressure field.

The idea of estimating the change in wake dissipation at a given axial location, by calculating $C_{\dot{E}}$ on each integration area, is an engineering approximation. This approach is an extension to the one adopted by Hall [23], who calculated this quantity for a flow through nacelle placed at the end of the D8. While the notion of calculating $C_{P_{K_{in}}}$ and η_{PR} at different axial stations makes sense from a physics perspective, as these are 'local' quantities, the same is not quite as valid for $C_{\dot{E}}$. The wake starts at the trailing edge of the fuselage (or any other body like the wing for example), and thus, only the measurement at the A1.00 is valid from both the physics and the engineering approximation viewpoints. Keeping this in mind, the $C_{\dot{E}}$ trends should be considered in the sense that these values represent an *engineering approximation* of what the wake dissipation benefit would be, if the fuselage was truncated at that axial station and an engine was placed at that location to ingest part of the wake.
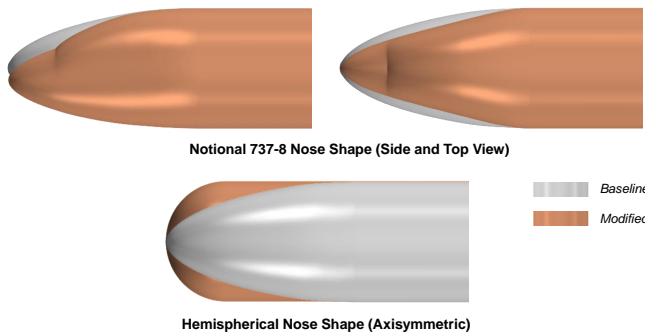
3. Sensitivity to Aircraft Angle of Attack

Running the baseline geometry at $\alpha = 2°$ changes the inviscid flow field. The boundary layer growth over the fuselage surface is no longer axisymmetric, with a thicker boundary layer seen at the 90° and 45° stations. This difference in the boundary layer thickness accounts for the increase in $C_{P_{K_{in}}}$ and decrease in η_{PR} relative to case 1.1 at most axial stations. The A1.00 station shows opposite trends to the other stations due to the overall upward shift in the boundary layer at a positive angle of attack. This flow feature is clearly illustrated in Fig. 9, which shows the η_{PR} contours at the A1.00 station for both case 1.1 and 1.2. In this figure, one can see that the integration area captures a larger portion of high total pressure flow at $\alpha = 2°$ than at $\alpha = 0°$. The trends for $C_{\dot{E}}$ are flipped relative to the other two BLI effects, where the 0° stations show more change rather than the 90° stations. This observation can be attributed to the significant change in the w velocity component at the 0° stations, thereby favoring the perturbation kinetic energy component of $C_{\dot{E}}$.
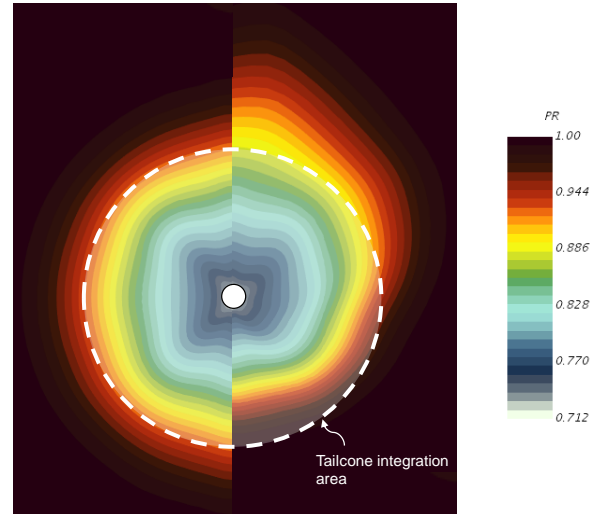
Fig. 9 **Effects of angle of attack on the boundary layer at the A1.00 station**

B. Experiment 2: Sensitivity to Fuselage Nose Design

1. Experimental Overview

Fig. 10 **Experiment 2: fuselage nose shapes**

The following experiment aims to test the governing hypothesis on changes to the fuselage nose shape. Rather than defining a few detailed parameters for the nose and systematically varying them, the sensitivity of the BLI effects to the nose can be efficiently assessed using two distinct geometries. Fig. 10 shows the different geometries used for the nose shape (orange), relative to the baseline in gray. The baseline geometry has a smooth elliptical (and axisymmetric) nose shape. Most existing passenger aircraft, however, do not have axisymmetric noses. Case 2.1 aims to compare a typical nose shape to the existing baseline. OpenVSP and three-view drawings of the 737-8 from [24] are used to recreate this nose shape, modified slightly to match the baseline geometry center-body diameter. The geometry change does not produce any significant pressure effects like shocks or separation and is thus a 'small' perturbation to the nose. If the influence of this modification is indeed local, then any shock free perturbations should also be limited, which avoids the need for running additional cases if the propulsor stations of interest are outside this localized influence. Case 2.2 on the other hand represents the nose shape as a hemisphere. This shape is the simplest representation of the nose, however, the less gradual change in curvature produces a shock at high subsonic Mach numbers and is thus a 'large' perturbation. Case 2.3 is conducted to assess whether the results from case 2.1 also hold at $\alpha = 2°$.

2. Results and Discussion

Fig. 11 shows the differences in the calculated BLI effects for trials 2.1, 2.2 and 2.3 relative to the baselines. These trends are expressed in dimensional power and equivalent force relative differences for $C_{P_{K_{in}}}$ and $C_{\dot{E}}$, while the pressure recovery changes are expressed as percentage differences[†]. The thresholds for significant changes are shown with black lines. From Fig. 11a, it is apparent that significant changes in the BLI effects are limited to the first 10% of the fuselage,
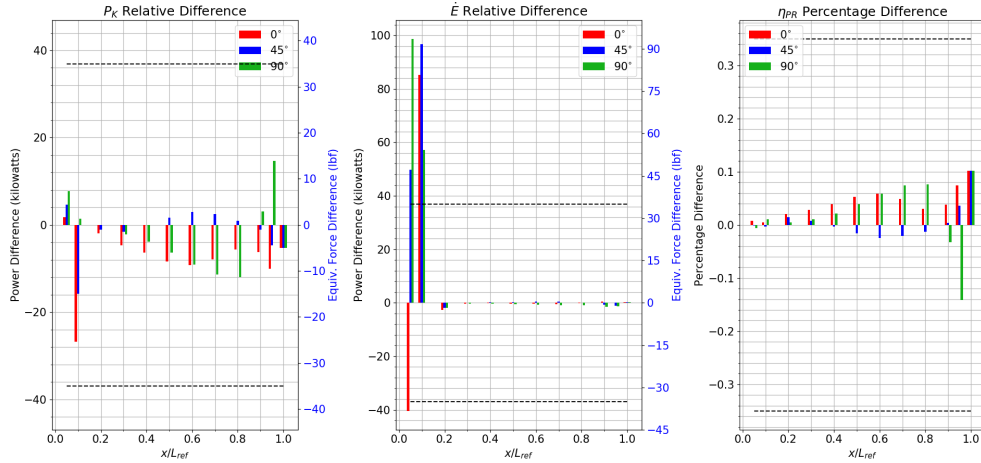

[†]In figures that compare case j vs. case i, the relative difference between case j and i is calculated as $\Delta_{ji} = (\cdot)_j - (\cdot)_i$. This relative difference is expressed in terms of power ($\Delta_{ji} \times q_\infty V_\infty S_{ref}$) and an equivalent force ($\Delta_{ji} \times q_\infty S_{ref}$). The percentage difference for η_{PR} is given by $\frac{\Delta_{ji}}{(\cdot)_i} \times 100\%$.
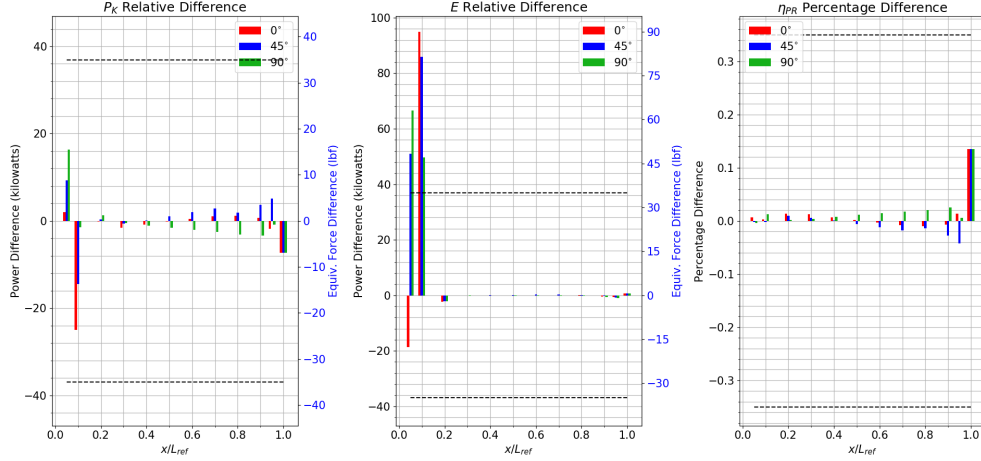
(a) E2.1 vs. E1.1 ($\alpha = 0°$ Baseline)
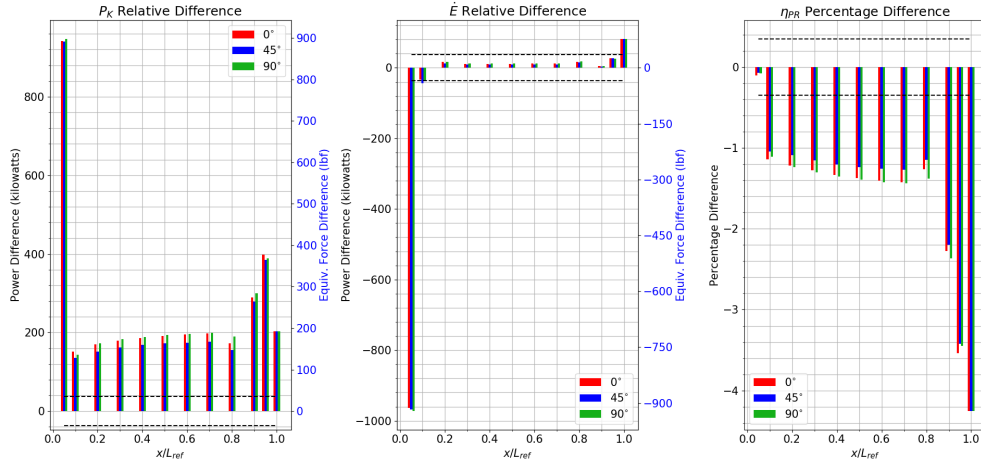
(b) E2.2 vs. E1.1 ($\alpha = 0°$ Baseline)

(c) E2.3 vs. E1.2 ($\alpha = 2°$ Baseline)

Fig. 11 Experiment 2: differences in estimates of the BLI effects due to changes in fuselage nose shape

i.e., in the region of the nose. The change in $C_{\dot{E}}$ is more pronounced than the change in $C_{P_{K_{\text{in}}}}$, while the change in pressure recovery is insignificant. Pressure recovery is solely dependent on the viscous losses in the boundary layer,

given the absence of shocks, and thus this result is indicative of minimal changes to the boundary layer itself as a result of the nose shape perturbation. Propagation of the disturbances downstream decays quickly. The differences in the BLI effects are well below the thresholds and are thus insignificant, supporting the theoretical reasoning behind the hypothesis. Similar results are obtained at $\alpha = 2°$, shown in Fig. 11c.

Now consider case two. The relative differences in the BLI effects seen in Fig. 11b all exceed the critical threshold, except for $C_{\dot{E}}$ in the center-body region. This trend is due to the presence of a shock just behind the A0.05 station. The adverse pressure gradient across the shock, and the subsequent thickening of the boundary layer have a favorable impact on $C_{P_{K_{in}}}$, but are naturally detrimental to η_{PR}. The favorable pressure gradient in the nose region and high flow acceleration increase the pressure defect work rate magnitude, which accounts for the significant $C_{\dot{E}}$ change at the nose. The pressure distribution downstream is similar to the baseline, but the thicker boundary layer increases the perturbation kinetic energy rate, resulting in a small, but net positive impact on $C_{\dot{E}}$.

The observations above support the governing hypothesis. A nose geometry change that causes a shock cannot be treated as a 'small' perturbation, since the impacts of this change are felt downstream across the entire length of the fuselage. Thus, one cannot arbitrarily default the nose geometry shape when generating surrogates of the BLI effects, if such a setting produces a shock. However, if the nose shape is defaulted to a shock free state, then the above results suggest that any shock-free perturbations to this shape will only show a localized impact on the BLI effects. As a consequence, for any engine location downstream of the nose, the detailed design variables defining the nose shape fall within the inactive variable set, given their negligible impact on the BLI effects. Thus, in the absence of design knowledge required to define the nose OML, a simplified (and shock free) representation of the nose can be used when generating surrogate models of the BLI effects.

C. Experiment 3: Sensitivity to Fuselage Aft Section Design

1. Experimental Overview

This experiment focuses on the impacts of the fuselage aft section on the BLI effects. The significance of tail cone design on BLI concept performance is emphasized by the number of shape optimization studies conducted, such as those by Gray [14, 18], Ordaz [30], and Kenway [12] for example. Given the impracticality of detailed and high fidelity aerodynamic optimization in early concept design, the objective of this experiment is to find the requirements for creating the simplest representation of the tail cone geometry that can be used for generating surrogates of the BLI effects in concept design.

The axisymmetric conical representation of the fuselage aft section is perhaps the simplest geometry model, but is not realistic compared to existing aircraft designs. Trial 3.1 therefore aims to quantify the discrepancy in the BLI effects calculated along the fuselage as a result of replacing this simple baseline aft section with an upswept tail cone commonly seen on aircraft. In doing so, both macro parameters like fuselage closure angle and upsweep angle are varied in addition to detailed parameters defining the OML curvature. This up-swept tail cone is created in OpenVSP using three
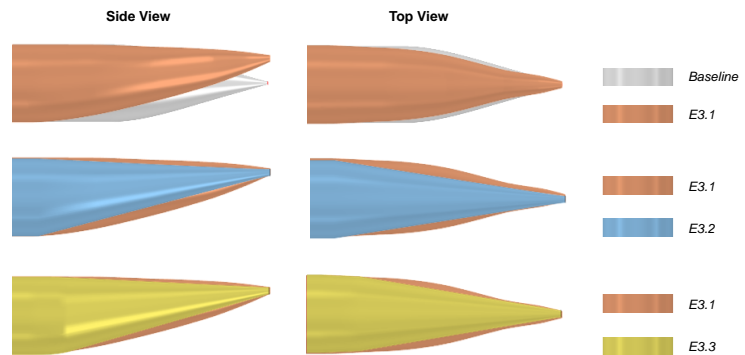

Fig. 12   Experiment 3: fuselage tail cone shapes

view drawings of the 737-8 from [24]. This geometry shown in orange in Fig. 12. Then, to isolate the impacts of the detailed parameters defining the aft end, trial 3.2 replaces the notional 737-8 tail cone with a simple lofted cone that approximately matches the upsweep and closure angles of the notional 737-8 geometry, shown in blue in Fig. 12. The transition between the fuselage cylindrical center-body and the conical upswept tail cone is sharp. A comparison between trial 3.1 and the baseline geometry quantifies the differences in the BLI effects largely due to a change in the aft end macro parameters. A comparison between trial 3.2 and trial 3.1 on the other hand quantifies the impact of the differences in the detailed design parameters of the tail cone. In case 3.3, the transition between the center-body and tail cone is arbitrarily smoothened out (a change in detailed design parameters), to assess whether the discrepancies in the BLI effects can be minimized. This geometry is shown in yellow in Fig. 12, and this case is also compared to trial 3.1.
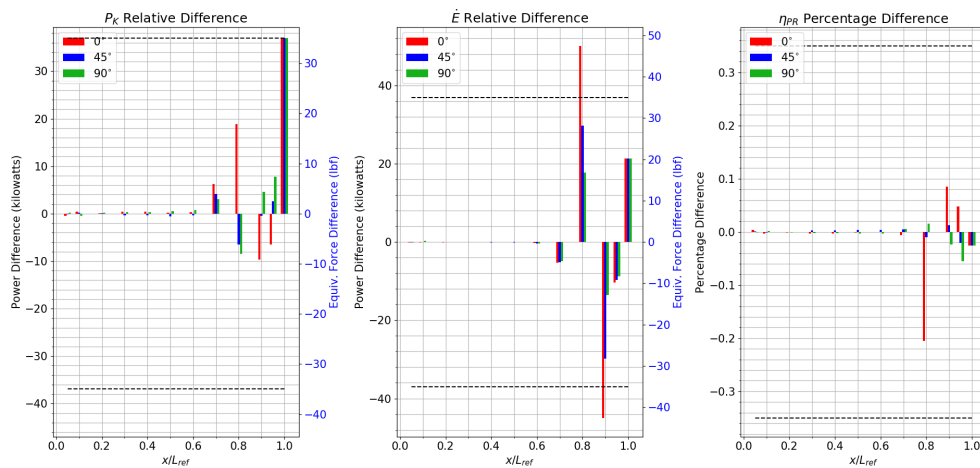
2. Results and Discussion
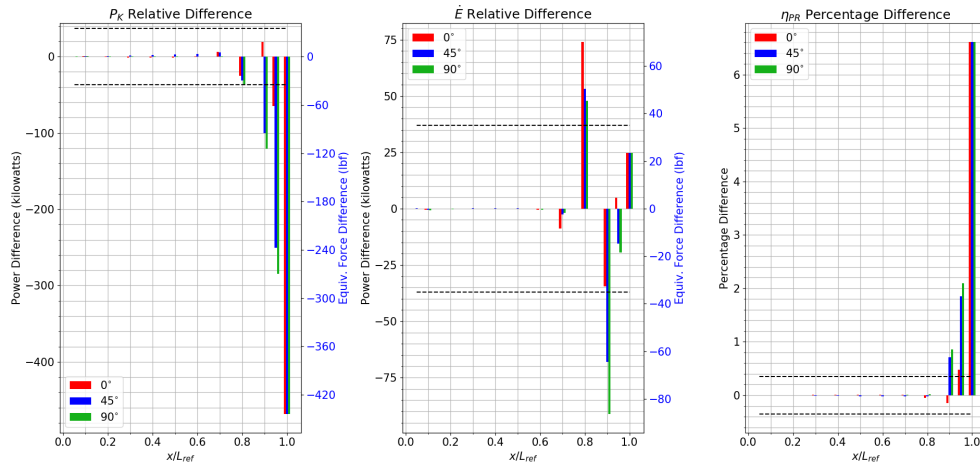
(a) E3.1 vs. E1.1 (Baseline)
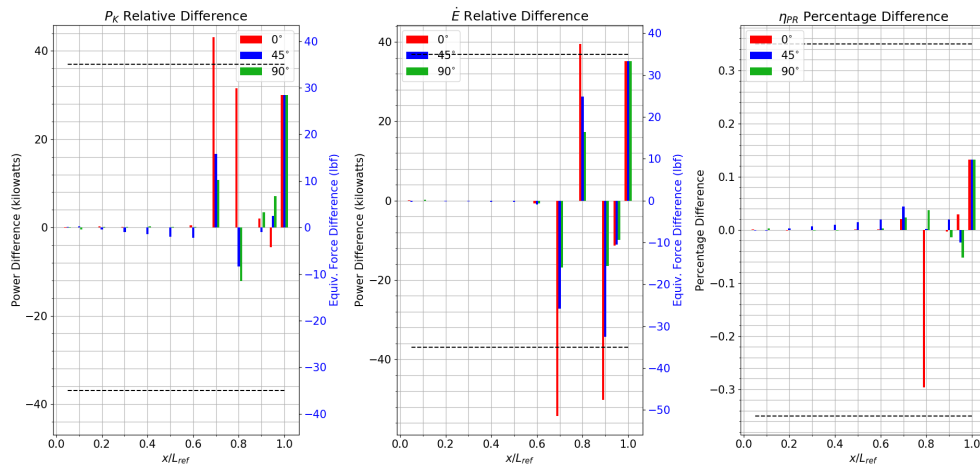
(b) E3.2 vs. E3.1

(c) E3.3 vs. E3.1

Fig. 13   Experiment 3: differences in estimates of the BLI effects due to changes in fuselage aft section shape

Fig. 13 presents differences in the BLI effects for the three comparison sets. Comparing trial 3.1 with the baseline

16

geometry (Fig. 13a), one can see that the upstream influence of the tail cone shape change is negligible, consistent with the theoretical reasoning in Sec. III . The differences are localized to the aft stations as expected, but exceed the critical thresholds quite significantly. Unsurprisingly, this finding indicates that an axisymmetric tail cone is an inadequate representation of a typical fuselage aft section. The differences in $C_{P_{K_{\text{in}}}}$ and η_{PR} relative to the baseline, at the 45° and 90° stations, are much larger than those at the 0° circumferential station. Given differences in slope of the geometry at the 90° stations, and to a lesser extent at the 45° stations, the boundary layer sees a less adverse pressure gradient in trial 3.1 than it does in 1.1. The boundary layer is thinner at these stations, which results in smaller $C_{P_{K_{\text{in}}}}$ and larger η_{PR}.

To ascertain the likelihood of the closure and up-sweep angles being the driving factors, case 3.2 is compared to case 3.1, shown in Fig. 13b. It is immediately obvious that by just roughly matching the closure and upsweep angles, the differences in the BLI effects are reduced by an order of magnitude, compared to the previous comparison. The differences in η_{PR} are below the threshold for all aft stations and while there are still some locations that exhibit higher than critical values for $C_{P_{K_{\text{in}}}}$ and $C_{\dot{E}}$, the extent to which these values exceed the threshold is much smaller than before. A consequence of having a sharp transition between the center-body and the tail cone is excessive flow acceleration at the corner, followed by a small separation bubble on the underside, This phenomena is illustrated in Fig. 14, which shows the axial velocity contours at the symmetry plane. This separation bubble creates a region of slow moving flow behind it, which most significantly affects the flow at the 0° circumferential station. The large differences in the BLI effects at the 70% and 80% span stations are a result of this flow behavior.
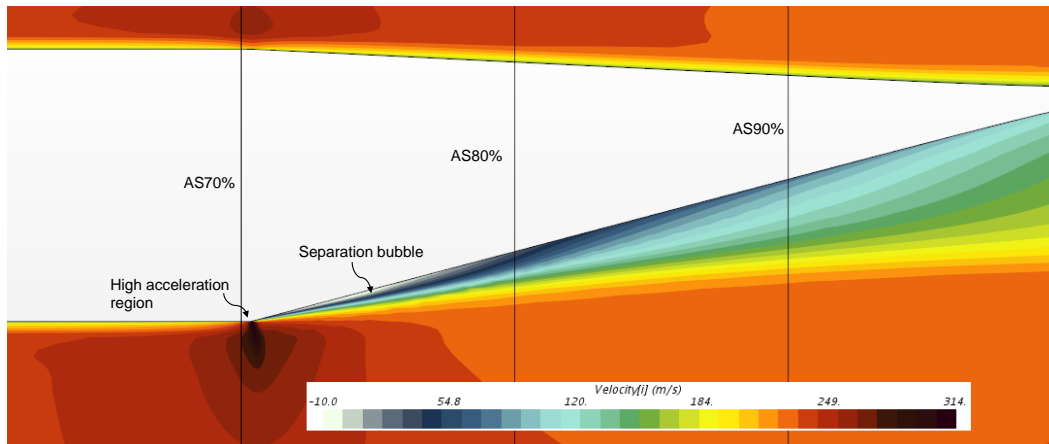
Fig. 14   Experiment 3.2: strong acceleration and flow separation around geometry transition corner (symmetry plane view, $V_\infty = 237$m/s)

To minimize this effect, an arbitrary curvature is applied to the transition region between the center-body and tail cone to smooth it out. The resulting geometry minimizes flow acceleration and eliminates the separation bubble seen previously. A comparison of the BLI effects between case 3.3 and 3.1 is shown in Fig. 13c. The differences in $C_{P_{K_{\text{in}}}}$ are now all below the thresholds, like η_{PR}, and the differences at the 70% and 80% span stations are also minimized. The net difference of $C_{P_{K_{\text{in}}}} + C_{\dot{E}}$ at the A1.00 station is also smaller than before.

From the above results, it can be concluded that as hypothesized, the macro parameters: upsweep and closure angles, indeed have a stronger influence on the BLI effects than the more detailed curvature. Given this relative influence, it is sufficient in a BLI concept design methodology to default the curvature to a setting that avoids adverse flow features, even though this setting may not be optimal. The discrepancy in the BLI effects between the optimized curvature geometry at the end of preliminary design and the default geometry used in concept design for generating the BLI effects surrogates will mostly be seen in the estimates for $C_{P_{K_{\text{in}}}}$ and $C_{\dot{E}}$, while the difference in pressure recovery will be minimal. The discrepancy due to defaulting the detailed parameters, however, will be smaller than the discrepancy caused by a mismatch in the macro parameters. The BLI concept designer must therefore keep track of the upsweep and closure angles even at the early stages of design. Design knowledge in the form of constraints (such as on the upsweep angle for tail strike avoidance) or previous experience, can help lock down values for these macro parameters. However, if this knowledge is unavailable and a fixed value for each parameter cannot be established, then the designer must include these variables as part of the BLI effects surrogate model generation process.

### D. Experiment 4: Sensitivity to Presence of Belly Fairing

1. Experimental Overview

This experiment assess the significance of adding a belly fairing to the geometry model on the BLI effects. This fairing, shown in Fig. 15, is also used in experiment 6 with a wing, and thus serves as a baseline reference for those trials. The size of the fairing geometry is estimated based on an approximated wing root chord length for a 180 pax class vehicle. This geometry is analyzed at both $\alpha = 0°$ and $2°$.
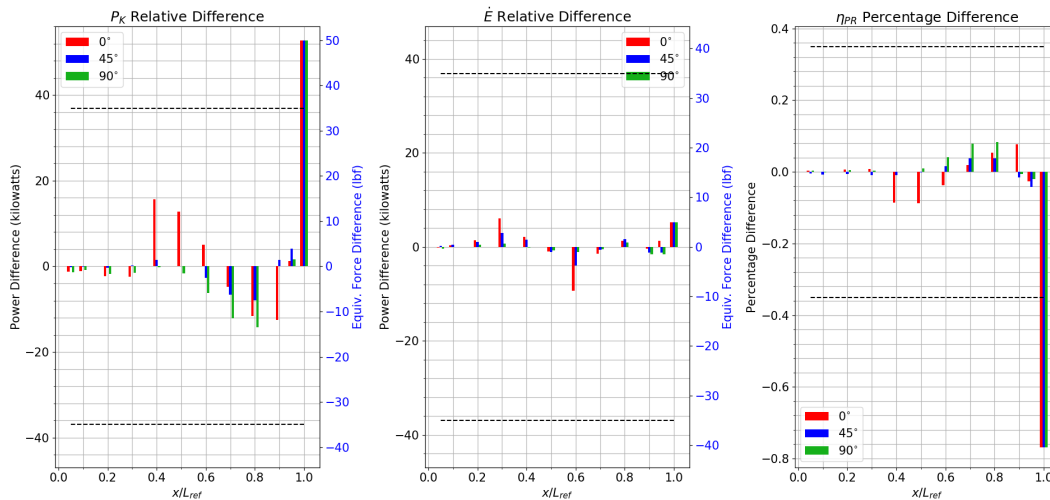

Fig. 15   Experiment 4: belly fairing geometry

2. Results and Discussion
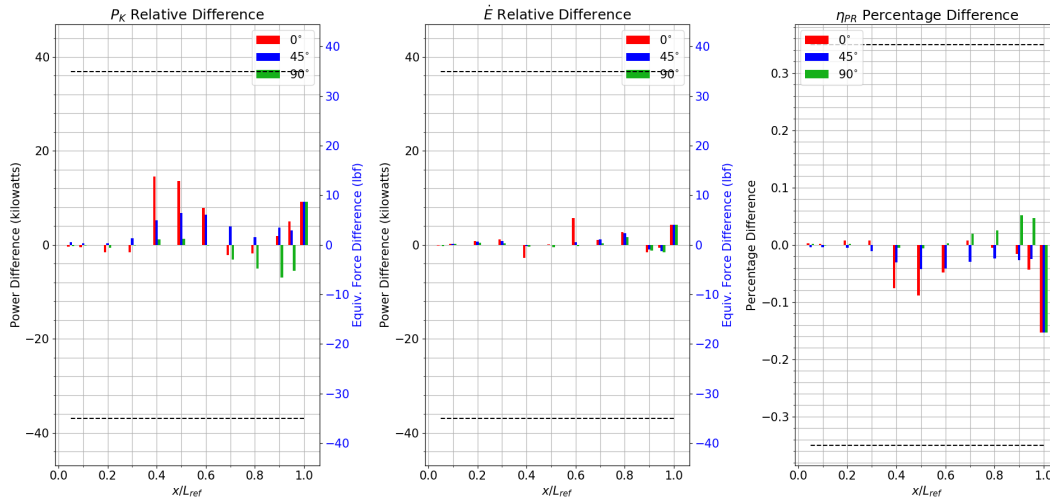

(a) E4.1 vs. E1.1 ($\alpha = 0°$ Baseline)

(b) E4.2 vs. E1.2 ($\alpha = 2°$ Baseline)

Fig. 16   Experiment 4: differences in estimates of the BLI effects due to addition of belly fairing

Fig. 16 shows the differences between cases 1 and 2, and the baseline at the two aircraft angles of attack. For the $\alpha = 0°$ case (Fig. 16a), the differences between the modified geometry and baseline are well below the critical

threshold. The $0°$ circumferential stations at 40% - 60% show the most sensitivity to the changes, given the proximity of the geometry perturbation to these measurement stations. The A1.00 station also exhibits some noticeable differences, given that it ingests the entire circumferential extent of the aft boundary layer, with fairing falling within the zone of dependence at this location. The fairing deflects the flow in the z direction, as seen in Fig. 17a. Here, streamlines emanating from the same source are compared across cases, with the baseline streamlines shown in black, and the fairing streamlines shown in red. The change in $z-$momentum results in a thicker boundary layer at the fuselage trailing edge, which accounts for the increase in $C_{P_{K_{in}}}$ and decrease in η_{PR} seen in Fig. 16. These differences are magnified at $\alpha = 2°$ (Fig. 16b), where the streamline deflection, relative to the $2°$ baseline, is more significant. This observation is also highlighted in Fig. 17b, which compares η_{PR} contours for the belly fairing geometry to the baseline at the A1.00 station. Note the region of low η_{PR} within the integration area at A1.00, for $\alpha = 2°$, that is not present in the baseline.
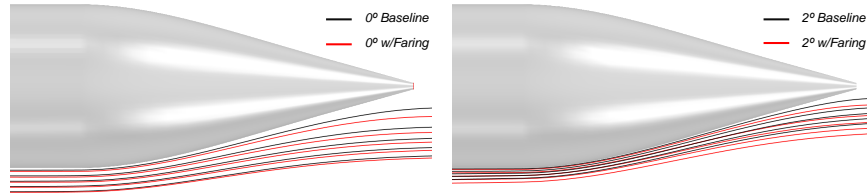
(a) Comparison of streamline deflections
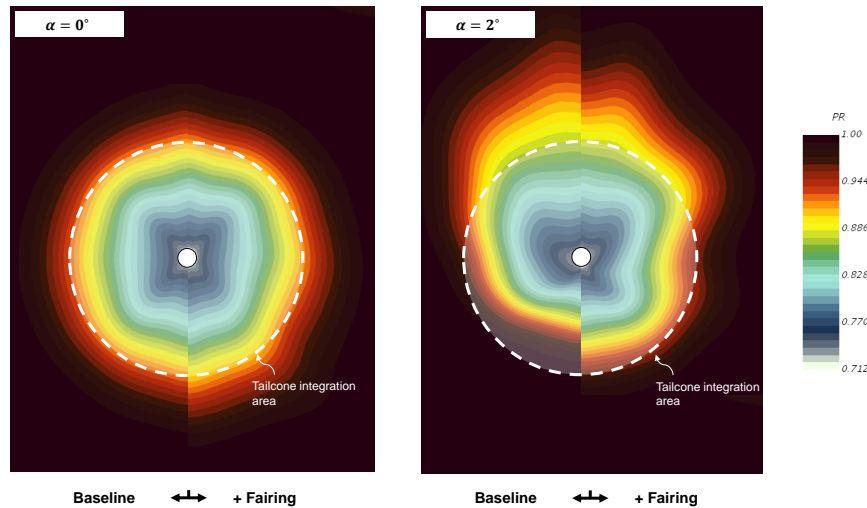
(b) Comparison of pressure recovery contours at A1.00

Fig. 17   Experiment 2.4: effects of belly fairing on flow field at the fuselage trailing edge station

The results indicate that the belly fairing has a relatively negligible impact on the BLI effects, except at the fuselage trailing edge station for a typical cruise angle of attack. While these results suggest that the fairing can be omitted from the geometry model, this conclusion is erroneous when the entire vehicle configuration is considered, rather than just the fuselage. As will be discussed in experiment 6, the fairing is necessary when including the wing in the geometry model. The fairing has an indirect impact on the BLI effects by mitigating significant flow separation that arises at wing-fuselage junction, and its downstream impact. As a consequence, the fairing minimizes the contribution of the wing at the $0°$ circumferential stations aft of it.

E. Experiment 5: Fuselage Shape and Slenderness Ratio Studies

1. Experimental Overview

In the following experiment, the fuselage as a whole is considered. The relative significance of the fuselage cross sectional shape (detailed parameter) vs. the fuselage cross sectional area and length (macro parameters), on the BLI

effects, is compared. The baseline geometry is scaled in the *x*, *y* and *z* directions to vary the cross sectional shape, area, and length for a given case. While these parameters can be arbitrarily set, the scope of this experiment is restricted to reasonable geometry perturbations, bounded by existing tube and wing aircraft designs. As such, the upper bounds on the center-body cross sectional area and overall fuselage length are from the Airbus A350 (a large twin-aisle aircraft), with approximate dimensions obtained from the airport planning document [31]. The lower bound is the baseline geometry, modeled on the Boeing 737-8. The variability in cross section shape is obtained from the B737-8 and A350, but the D8 cross sectional shape is also considered in these experiments. This shape, common to both the D8 and the NOVA-BLI, is representative of an unconventional cross section given its highly elliptical definition. Table 1 presents the eight geometry cases considered in this experiment. Recall, the baseline fuselage length, L_x = 39.12m and the center-body diameter $L_y = L_z$ = 3.89m. Elliptical cross-sectional shapes are obtained by scaling the entire geometry in the *y* and *z* directions. A total of eight comparisons are made, illustrated in Fig. 18.

Table 1   Experiment 5: Overview of Cases

Experiment	L_x (m)	L_y (m)	L_z (m)	Center-body	Notional Source
5.1	39.12	3.76	4.01	Elliptical	B737-8 Cross Section
5.2	39.12	5.96	6.09	Elliptical	A350 Cross Section (CS)
5.3	39.12	6.03	6.03	Circular	A350 Avg. CS
5.4	72.25	5.96	6.09	Elliptical	A350 CS & Length
5.5	72.25	6.03	6.03	Circular	A350 Avg. CS & Length
5.6	72.25	3.89	3.89	Circular	A350 Length
5.7	39.12	5.36	3.95	Elliptical	D8 CS
5.8	39.12	4.60	4.60	Circular	Avg. D8 CS

Comparisons 1-4 assess the significance of the detailed fuselage shape parameters on the BLI effects. The simplest representation of the fuselage is a circle, which is defined by a single parameter i.e. the diameter. Most conventional aircraft, however, have elliptical cross sections, as illustrated in Fig. 18. Elliptical shapes require two parameters, which adds a degree of uncertainty in early conceptual design. The cross sectional area is an important parameter for transonic aircraft and defining the area sets the diameter for a circular approximation of the fuselage. However, in the case of an elliptical cross section, different combinations of the major and minor axes lengths can generate the same cross sectional area. While other design constraints eventually help define the values of these detailed parameters, this design knowledge may not be available in the early stages. Thus, when generating surrogate models of the BLI effects using CFD, the question arises whether this shape even matters. By comparing the BLI effects for the elliptical cross section to the circular approximation, one can assess the significance of the fuselage shape on the results. If the differences are negligible, then one can get away with the simpler geometry model with minimal loss in accuracy. As shown in Fig. 18, the length of the fuselage, L_x and cross sectional area, A_{CS}, are held constant for a given comparison. Comparisons 5-8 assess the significance of varying the macro parameters on the BLI effects. For each of these cases, the circular approximation of the fuselage shape is used.

2. Results and Discussion
Fig. 19 presents the relative differences in the BLI effects for comparisons 1-4. Looking at the plots for comparisons 1-3, i.e., for conventional cross section shapes vs. circular approximations, the differences in the BLI effects are well below the critical thresholds. In comparisons 1 and 3, the slenderness ratio of the fuselage is large enough to not cause a shock. However, by increasing the cross sectional area and keeping the length constant, the slenderness ratio decreases in comparison 2, causing a shock just aft of the nose. Even in this scenario, the difference between a circular and elliptical cross section is negligible. Thus, one can conclude that for conventional elliptical configurations where the final cross section shape parameters are expected to fall within a range of $0.94 \leq \frac{L_y}{L_z} \leq 1.00$, the additional parameter needed to create an elliptical shape is not necessary for modeling the BLI effects in early conceptual design. One can safely use a circular cross section geometry model since the error in doing so is negligible. However, when considering an unconventional configuration like the D8 or the NOVA-BLI, this simplification is challenged as the differences between a circular approximation and the elliptical shape are more pronounced, as seen in Fig. 19g. Despite the
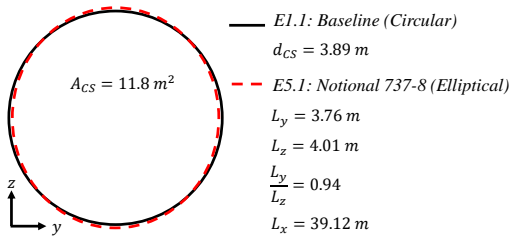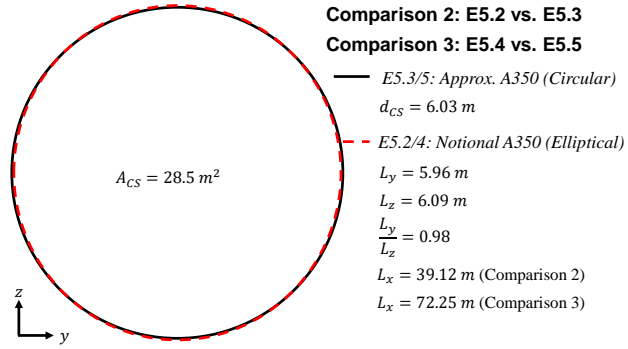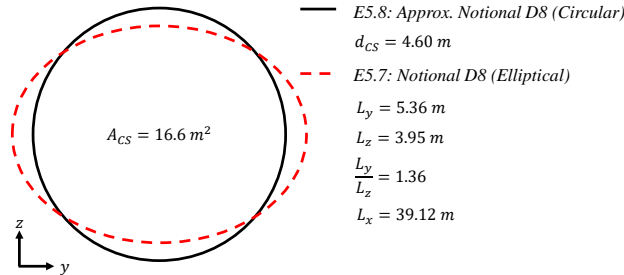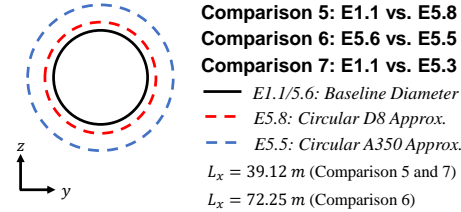
Fig. 18 Experiment 5: comparisons 1-4 assess the impacts of detailed fuselage shape parameters, while comparisons 5-8 establish the significance of cross sectional area and overall fuselage length

relatively exaggerated results, it is interesting to note that most the differences still fall within the critical thresholds, with only the values at the A0.95 and A1.00 stations showing differences that exceed the thresholds. The differences at the A0.90 station, though within the thresholds, are still appreciable. In short, the results at the tail cone stations are the most sensitive to the fuselage shape. This is no surprise, as the results from experiment 3 indicated as much. Fig. 20 compares the tail cone geometries in comparison 4.
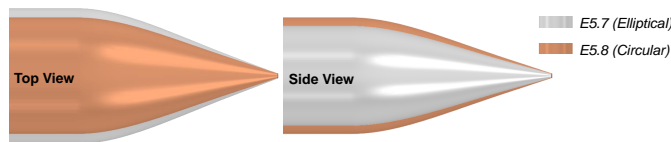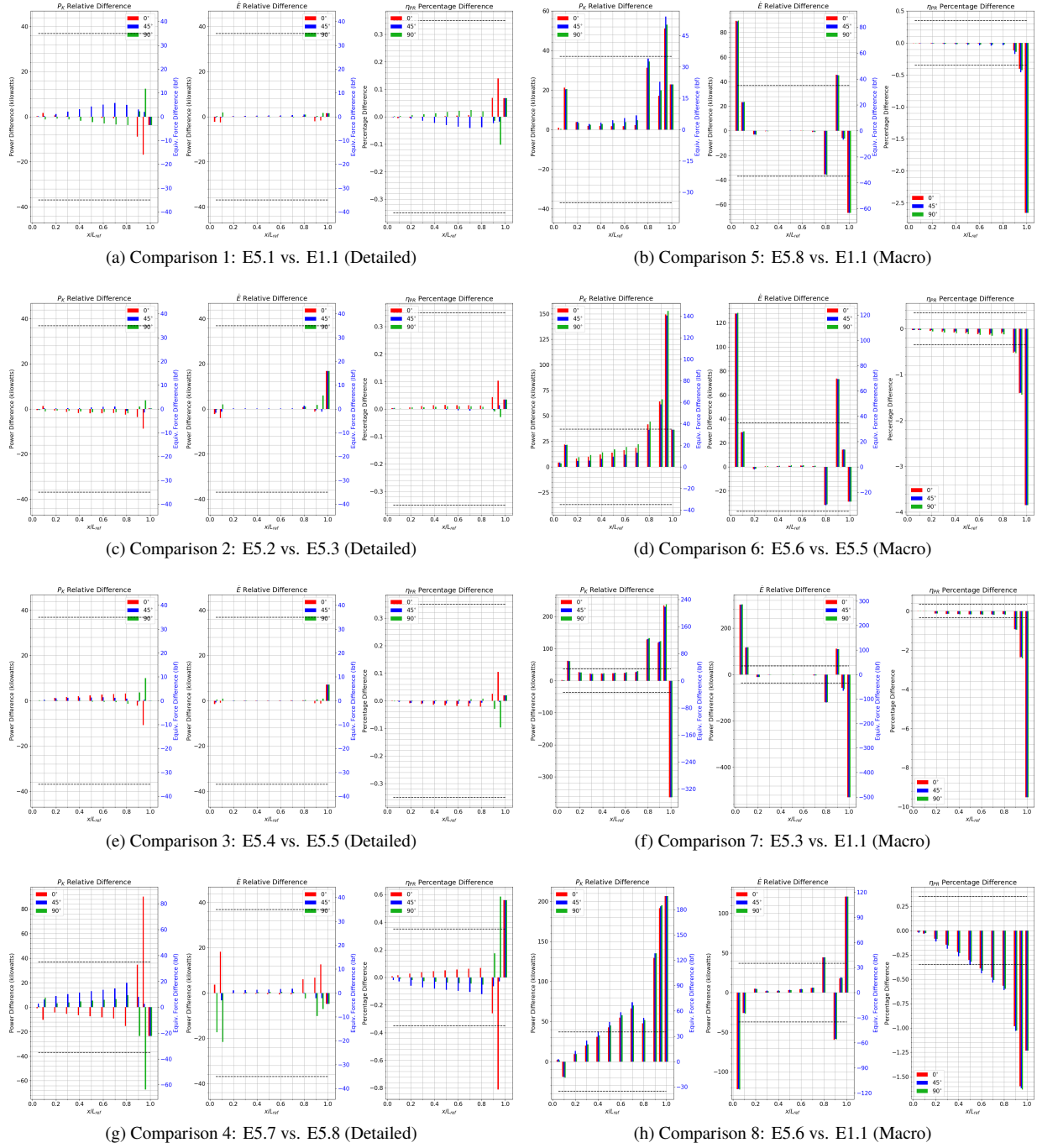

Fig. 20 Comparison of 5.7 and 5.8 tail cone geometries

Evident from the geometries, the fuselage closure, upsweep, and upper surface angles for the two geometries are not the same. In changing the fuselage shape, the macro parameters defining the tail cone design were not held the same, accounting for the differences seen in this region in Fig. 19g. Given this result, the designer has a two options to consider when coming up with a simplified geometry for a highly elliptical configuration in concept design:

1) Use an elliptical shape for the entire cross section. If the values for L_y and L_z are unknown, it is sufficient to define an *appropriate* range on these parameters (constrained by the cross sectional area requirements), and then set one term to the center point value and calculate the other based on the cross sectional area requirement. Based on the results from comparisons 1-3, the variation in the BLI effects due to a difference in the values set for L_y and L_z, within the previously defined range, is likely to be minimal.

2) Use a circular shape for the fore-body, but gradually loft to an elliptical cross section for the tail cone.

In both the options above, it is necessary to account for the effects of the tail cone and fuselage macro parameters. Either these parameters need to be set to the correct values in the CFD geometry model, or, varied as part of the

21

(a) Comparison 1: E5.1 vs. E1.1 (Detailed)

(b) Comparison 5: E5.8 vs. E1.1 (Macro)

(c) Comparison 2: E5.2 vs. E5.3 (Detailed)

(d) Comparison 6: E5.6 vs. E5.5 (Macro)

(e) Comparison 3: E5.4 vs. E5.5 (Detailed)

(f) Comparison 7: E5.3 vs. E1.1 (Macro)

(g) Comparison 4: E5.7 vs. E5.8 (Detailed)

(h) Comparison 8: E5.6 vs. E1.1 (Macro)

Fig. 19 Experiment 5: differences in estimates of the BLI effects, due to changes in fuselage cross sectional shape representation (elliptical vs circular), cross sectional area, and length

surrogate model generation process. The first option is ideal for configurations like the D8 where it may be difficult, or impossible, to capture the closure and upsweep angles, and obtain the correct cross sectional area of the tail cone using a simple circular cross section.

The impacts of varying the fuselage cross sectional area and the length are also shown in Fig. 19. Comparisons 5 and 6 are for shock free cases, where the reference case cross sectional area is at the baseline value of 11.8m^2 and the comparison geometries' areas are at 16.6m^2 and 28.5m^2 respectively. Increasing the area increases the magnitude of the

differences in the BLI effects at most stations. These differences are even more pronounced in the presence of a shock, seen in comparison 7. This shock is caused by a reduction in the slenderness ratio going from the baseline diameter to the diameter of the circular approximation for the notional A350, for the baseline geometry length. In comparisons 5 and 6, η_{PR} variations upstream of the tail cone stations are negligible. This is because changes to fuselage diameter upstream have a more direct impact on the inviscid flow field than on the boundary layer. If there is no shock, the pressure recovery changes upstream are minimal. In comparison 7, the shock presents another source of losses, resulting in a decrease in η_{PR}. Even though the differences upstream are below the critical threshold, the magnitude of these differences in comparison 7 is much larger than those in comparisons 5 and 6. The large differences in the tail cone region for all three comparisons are due to variations in the closure and upsweep angles of the tail cone due to changes in the fuselage area, and for the A1.00 station, due to changes in the fuselage trailing edge area (hub area). Comparison 8, shown in Fig. 19h, highlights the impacts of fuselage length on the BLI effects at a given axial station. A longer fuselage implies a thicker boundary layer at the same non dimensional axial station, accounting for the increase in $C_{P_{K_{\mathrm{in}}}}$ and decrease in η_{PR}.

The results from the above experiments provide some guidelines regarding the requirements for the geometry model from which surrogates of the BLI effects using CFD are generated. It can be seen that the macro parameters of the fuselage i.e. length and cross sectional area need to be defined correctly, or varied in the surrogate models given the sensitivity of the BLI effects to these parameters. The significance of the macro parameters of the tail are also emphasized in these trials, supporting the findings from experiment 3. With regards to the shape of the fuselage, it was found that the significance of such detailed parameters was minimal for conventional cross sectional fuselages, and that a circular approximation could be used. For unconventional highly elliptical cross sections, even though most of the errors are below the critical thresholds, it is recommended that an elliptical cross sectional shape be used. A circular approximation in this case may not be adequate to set the correct values of the tail cone angles and could compound the errors in the BLI effects estimates. Ranges on the values for the major and minor axes lengths of this elliptical shape will be constrained by the ranges on cross sectional area, tail cone closure, and upsweep angles.

F. Experiment 6: Sensitivity to Wing Design

1. Experimental Overview

As stated previously, studies in literature detected the impact of wing downwash on the distortion profile at the aerodynamic interface plane of the STARC-ABL BLI propulsor [12, 18]. These findings emphasized the need to include the wing in the vehicle model for that concept. This experiment aims to corroborate those findings and also generalizes the approach by considering other propulsor locations. This generalization allows one to draw conclusions regarding the importance of the wing on the BLI effects for concepts similar to the D8 and the NOVA-BLI. Specifically, the objective is to verify that the axial and circumferential location of the engine determines the contribution of the wing to the ingested boundary layer properties, as stated in the governing hypothesis. A secondary goal of this experiment is to quantify the relative sensitivity of the BLI effects to key macro and detailed parameters of the wing. Doing so would allow the designer to default potentially inactive wing design variables, thus reducing the dimensionality of the problem when generating surrogates of the BLI effects.

The primary objective of this experiment can be achieved by comparing the differences in the BLI effects at all measurement stations between a fuselage only baseline, and the same geometry with a reference wing. For this experiment, the Common Research Model (CRM) wing [32] is used. The original CRM wing is scaled down to a planform area of 130m^2, which is roughly comparable to the wing on the 737-8. The secondary objective of this experiment can be achieved by changing key wing design variables one at a time and comparing the measurements of the BLI effects for each perturbation to the reference wing case. Table 2 shows the main wing design variables considered as part of the scope for this experiment, the reference wing values, and the settings for the perturbed geometries. The macro parameters are those defining the wing planform and location, while the detailed parameters considered are the airfoil thickness and camber. These variables are chosen primarily because they represent major design parameters for aerodynamic performance and stability, with the planform variables in particular featuring as part of vehicle concept design studies. The axial location of the wing root leading edge at the symmetry plane is estimated from the airport planning document of the 737-8 [24].

A total of 10 cases are run, one for the reference wing, and one for each perturbation of the design variables. The last case applies all perturbations, except the camber, at once. Most of the perturbed values are chosen such that they fall on or within the bounds of a reasonable design space. Using the wing area for a conventional (non-BLI) 150-180

Table 2 Experiment 6: Design Variable Settings

Variable	Reference Wing	Perturbed Wing
Planform Area: S	130 m^2	160 m^2
Aspect Ratio: AR	9	7
Taper Ratio: λ	0.20	0.28
Leading Edge Sweep: Λ_{LE}	37°	20°
Dihedral: Γ	CRM	+5°
Axial Location (Wing Root LE): $\frac{x_{LE}}{L_{ref}}$	35%	30%
Max Thickness to Chord: $\left(\frac{t}{c}\right)_{max}$	CRM	+2%
Airfoil Camber	CRM	Modified CRM

pax aircraft, a variation of ±25% in this value can be reasonably expected as part of the sizing process with BLI and other technologies. As such, the perturbed wing area chosen is a 23% increase over the reference area. For context, the STARC-ABL concept proposed in 2016 featured a 38% increase in wing area relative to the N+3 Conventional Configuration (N3CC) [3]. The aspect ratio ranges obtained from [33] show that most aircraft fall within a range of 7-11. While current design trends favor high aspect ratios, a value of 7 for the perturbed case provides an estimate for the highest impact this variable can have on the BLI effects, given the stronger influence of the tip vortices on the flow around the fuselage. The perturbations for λ, Λ_{LE}, Γ and $\left(\frac{t}{c}\right)_{max}$ are based on common values for transport aircraft found in Raymer [34]. For λ, a typical range is 0.25 to 0.45. The middle point of 0.35 is a 40% increase from the lower bound. Since the baseline CRM λ is below this range, a 40% increase is applied to the reference value to obtain 0.28. The typical average Γ range is 0° to 10°. The average Γ for the reference wing is 4.5°. Thus, 5° is added to the dihedral values at each span station as a perturbation. The sweep angles for most transonic wings fall between 20° to 40°. Given that the CRM is near 40°, the perturbed wing is set to 20°. For the airfoil $\left(\frac{t}{c}\right)_{max}$, the reference wing average maximum thickness is 10.7%. The typical average values found in Raymer are between 10-14%. Thus, a positive delta of 2% is applied to each airfoil station to obtain the perturbed geometry. The airfoil camber is altered by changing two CST coefficients [35] on the lower surface of each airfoil, shown in Fig. 21.


Original

Modified

Near Wing-Fuselage Junction

Original

Modified
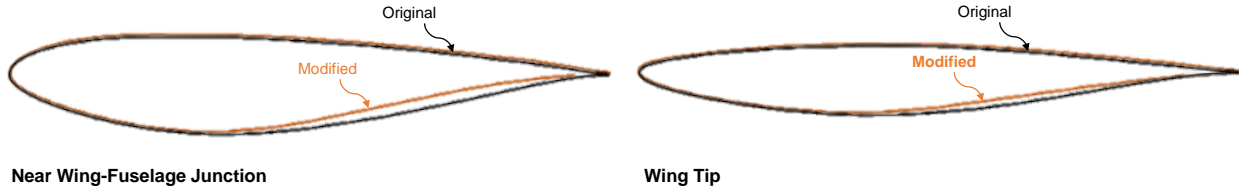
Wing Tip

Fig. 21 Camber variations shown for airfoils near the wing-fuselage junction and the wing tip

2. Results and Discussion

Initially, the reference wing was analyzed with the baseline fuselage without a fairing. Absence of the fairing, however, caused undesirable flow features, as shown in Fig. 22. Significant flow separation at the fuselage-wing junction is observed, at $\alpha = 0°$, as seen from the skin friction and x velocity contours. There is a region of slow moving flow behind the separation bubble, which appears to alter the effective body shape. This disturbed flow propagates to the trailing edge of the fuselage and beyond, highlighted in the pressure recovery contours at the 95% station in Fig. 22. A consequence of this flow feature is a significant favorable impact on $C_{P_{K_{in}}}$ and large decrease in η_{PR}, as seen in Fig. 23. In this figure, BLI effects trends from the baseline fuselage with a wing are compared to the fuselage only trends at $\alpha = 0°$. Results at the 40% and 50% stations are omitted since the integration areas intersect with the wing geometry, leading to erroneous measurements.

Given that these flow phenomena would likely bias the results, the belly fairing was subsequently included in all analyses. Doing so eliminated the excessive separation and downstream influence at both $\alpha = 0°$ and 2°. Fig. 24 compares the reference wing BLI effects at both 0° (Fig. 24a) and 2° (Fig. 24b) to the geometry from experiment 4.
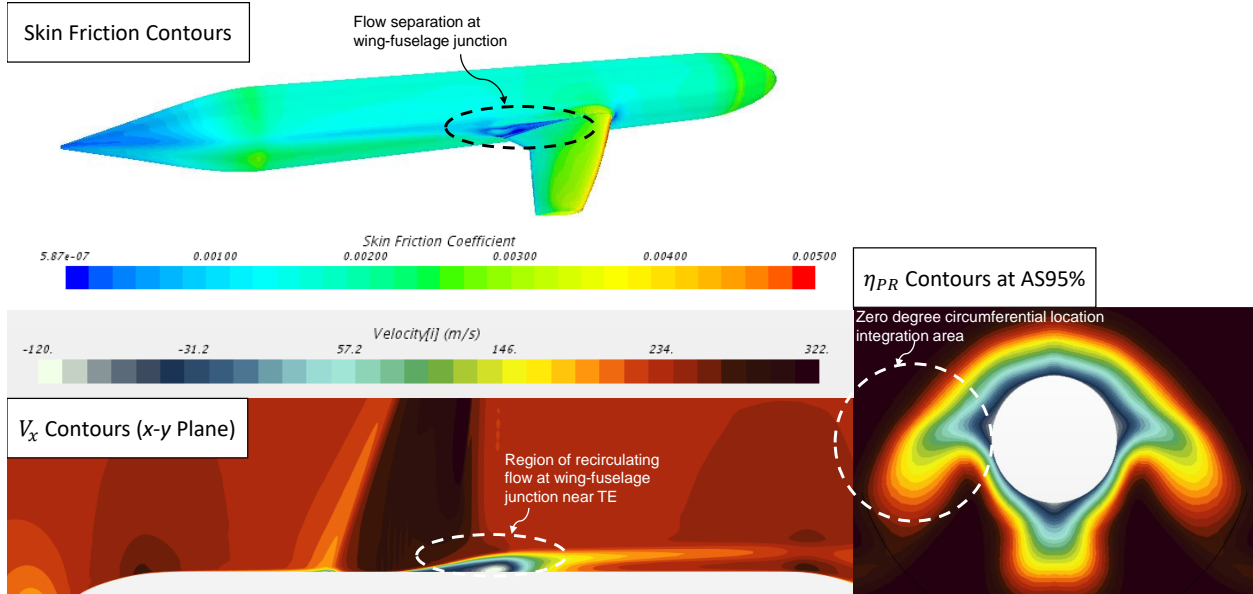
Fig. 22   Flow separation at wing-fuselage junction in the absence of a belly fairing

As shown previously, the fairing's impact is only significant at $\alpha = 2°$ at the A1.00 station. Thus, the trends shown are primarily driven by the presence of the wing. It is immediately apparent that the significant changes at the 0° circumferential stations are no longer seen. A more interesting observation is the larger difference at the 45° and 90° stations, particularly along the tail cone. Though initially counterintuitive, this observation highlights global influence of the wing on the flow field. In the absence of excessive separation, given the size of the integration areas and their relative location to the reference wing, the local influence of the reference wing wake is not as significant as the global effect through the induced downwash.
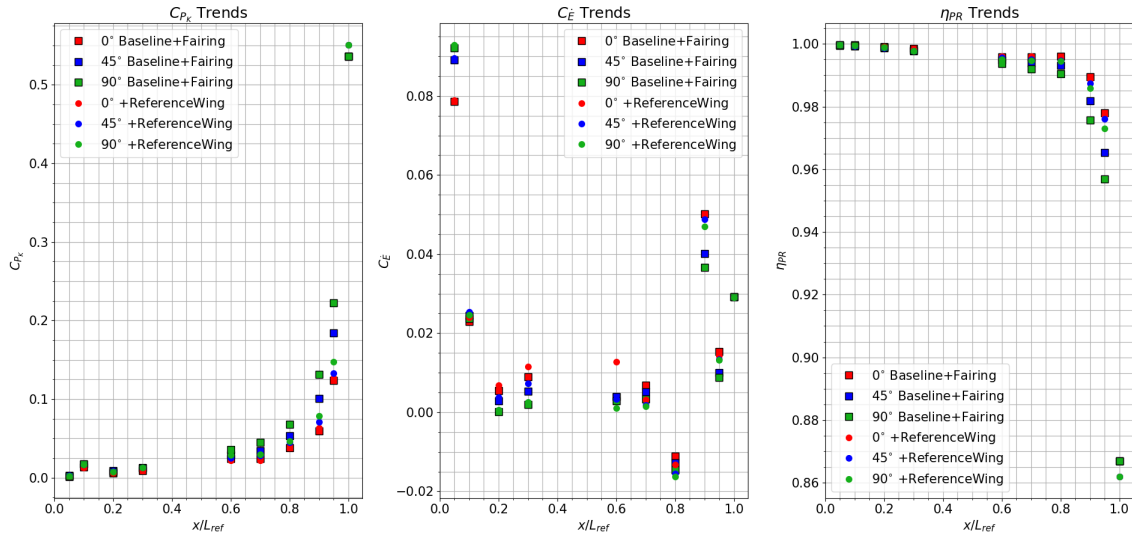
In Figs. 25a and 25b streamlines emanating from the same source, shown at the symmetry plane, are compared between the fuselage only (black) and wing case (red) for two angles of attack. The wing induced deflection of
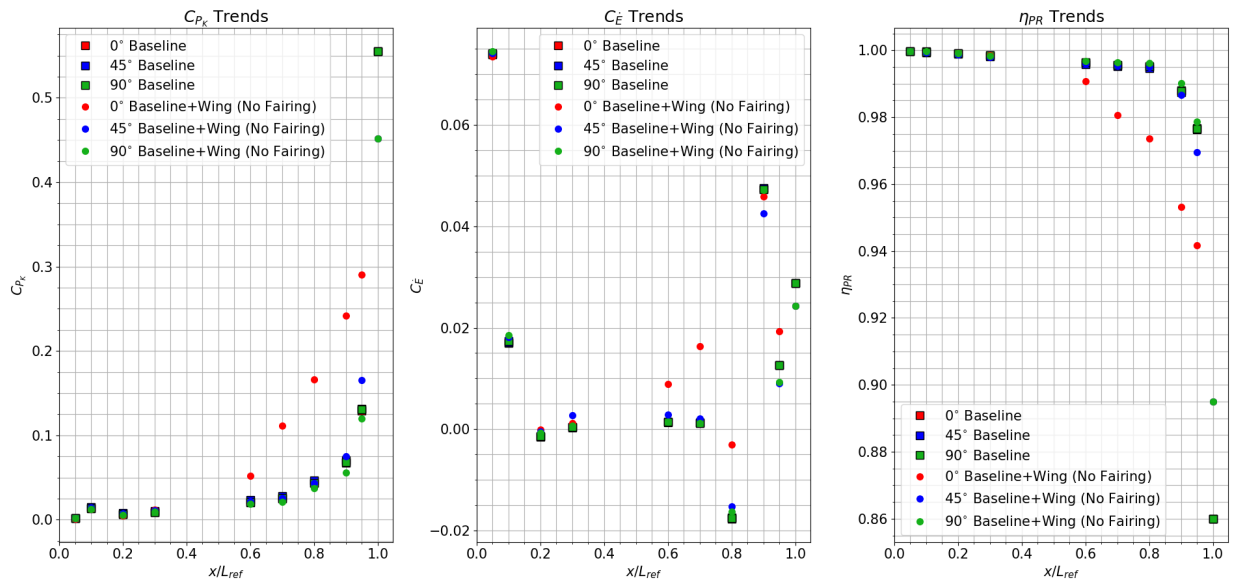
Fig. 23   Impact of the fuselage-wing separation on the BLI effects in the absence of a belly fairing
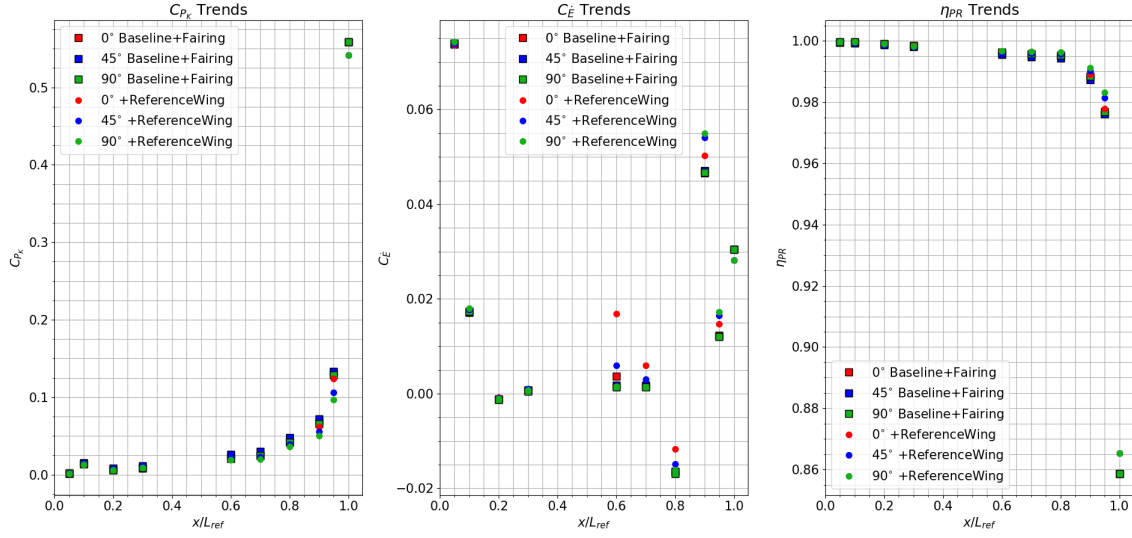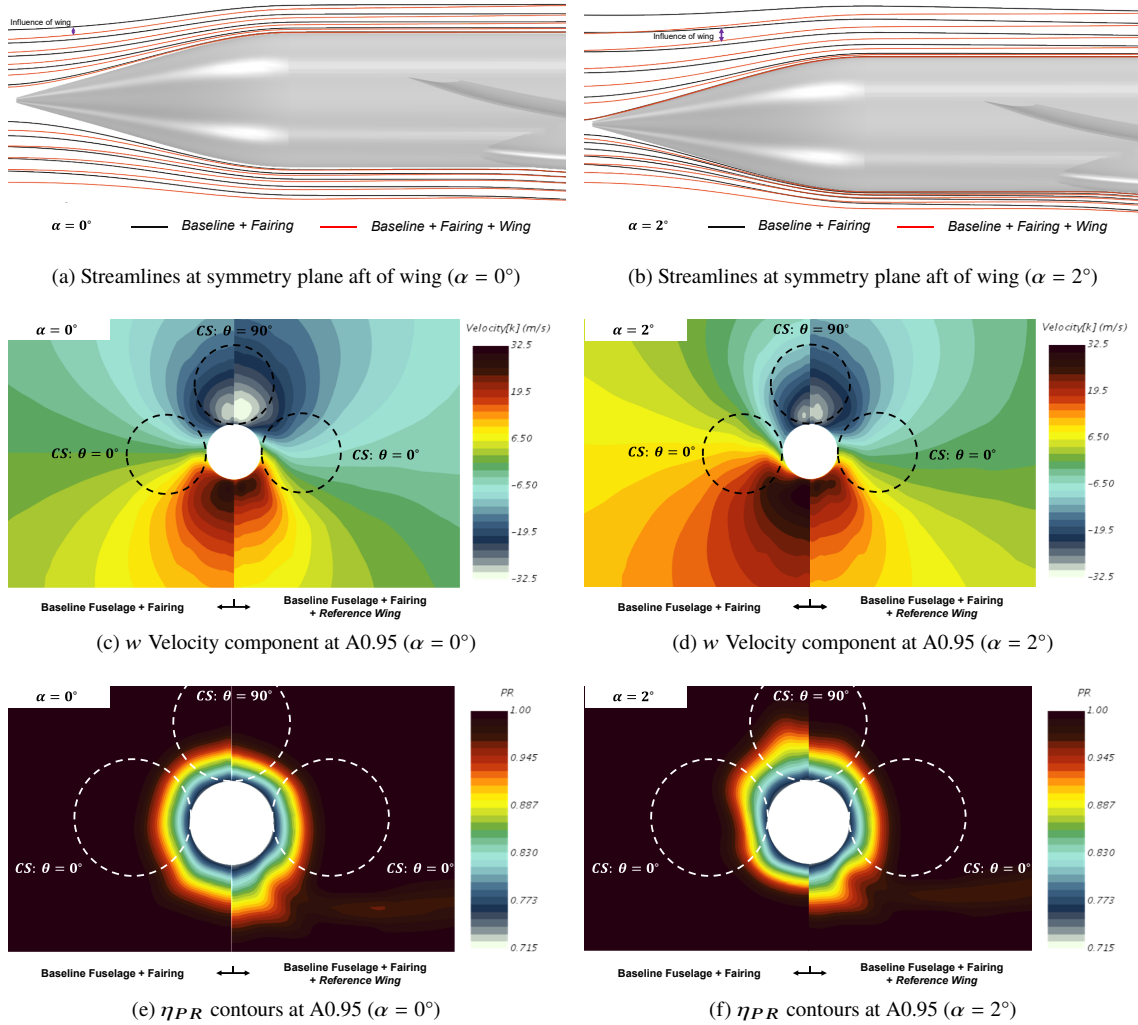
(a) E6.1v1 vs. E4.1 ($\alpha = 0°$ Baseline + Fairing)

(b) E6.1v2 vs. E4.2 ($\alpha = 2°$ Baseline + Fairing)

Fig. 24 Experiment 6: influence of the reference wing on the BLI effects with the belly fairing

streamlines in the negative z direction is evident from both these plots. A scalar view of the w velocity contours at the A0.95 plane in Figs. 25c and 25d illustrates the downwash variation in the $y - z$ plane in the vicinity of the fuselage. The integration areas at the 0° and 90° stations are shown in black. Notice the larger region of $-w$ flow at the 90 degree stations for the wing case compared to the baseline fuselage. Differences in w velocity are also observed at the 0° station, but the magnitude and thus the net effect on the BLI effects is smaller relative to the other circumferential stations. A thinner boundary layer at the 90° station is observed, evident from the η_{PR} contours in Figs. 25e and 25f, which explains the lower value of $C_{P_{K_{in}}}$ and higher value of η_{PR}, relative to the no wing case, seen in Fig. 24.

Relation between Wing Contribution to BLI Effects and Engine Location

Fig. 26 summarizes the results for all 10 wing cases, run at $\alpha = 2°$. In Fig. 26a, differences in the net BLI effect, $C_{P_{K_{in}}} + C_{\dot{E}}$, relative to the fuselage only case are shown in terms of an equivalent force. In Fig. 26b, the percent differences in η_{PR} relative to the no-wing baseline are presented. These figures compare the BLI effects aft of the wing,

26

(a) Streamlines at symmetry plane aft of wing ($\alpha = 0°$)

(b) Streamlines at symmetry plane aft of wing ($\alpha = 2°$)

(c) w Velocity component at A0.95 ($\alpha = 0°$)

(d) w Velocity component at A0.95 ($\alpha = 2°$)

(e) η_{PR} contours at A0.95 ($\alpha = 0°$)

(f) η_{PR} contours at A0.95 ($\alpha = 2°$)

Fig. 25   Experiment 6: influence of the reference wing on the flow streamlines, w velocity, and boundary layer

given that upstream differences are negligible. The bars in each plot are shown in the same order as shown in the legend. Results shown in these plots clearly support the hypothesis that the wing contribution to the BLI effects varies based on circumferential (and axial) location of the engine relative to the wing. The most significant influence of the wing is observed at the 90° stations, followed by the 45° and 0° stations. The magnitude of these differences grows along the axial distance for the 45° and 90° locations. Based on these results, it can be concluded that for concepts like the D8 that feature engines mounted on top in the last 10% of the fuselage, the wing must be included in the geometry model used for generating surrogates of the BLI effects. The discrepancy in the BLI effects estimates by omitting the wing is approximately 3-6 times the critical threshold for both $C_{P_{K_{in}}} + C_{\dot{E}}$ and η_{PR}, based on results at the A0.90C90 and A0.95C90 stations. The differences in BLI effects also exceed the critical thresholds at the A1.00 station, albeit to a lesser degree. Recall, the baseline geometry against which these differences are calculated includes the fairing. As seen in the results at A1.00 from experiment 4, the fairing itself has a positive contribution to $C_{P_{K_{in}}} + C_{\dot{E}}$ by about 55lbf and a negative impact on η_{PR} by about 0.76%, relative to the baseline fuselage geometry used in experiment 1.2. The wing contribution compounds the influence of the fairing at $\alpha = 2°$ for A1.00, such that the net difference between the wing/fairing/fuselage case relative to baseline fuselage is even larger. For the reference wing case, these differences are approximately 90lbf for $C_{P_{K_{in}}} + C_{\dot{E}}$ and -1.3% for η_{PR}. In summary, the results presented here also support findings in literature regarding the inclusion of the wing for concepts like the STARC-ABL.

For engines mounted at the 0° locations, trends show that the wing's contribution is below the defined critical thresholds, even for case 10 where all variables are set to their perturbed values. The outlier is at the 0° circumferential
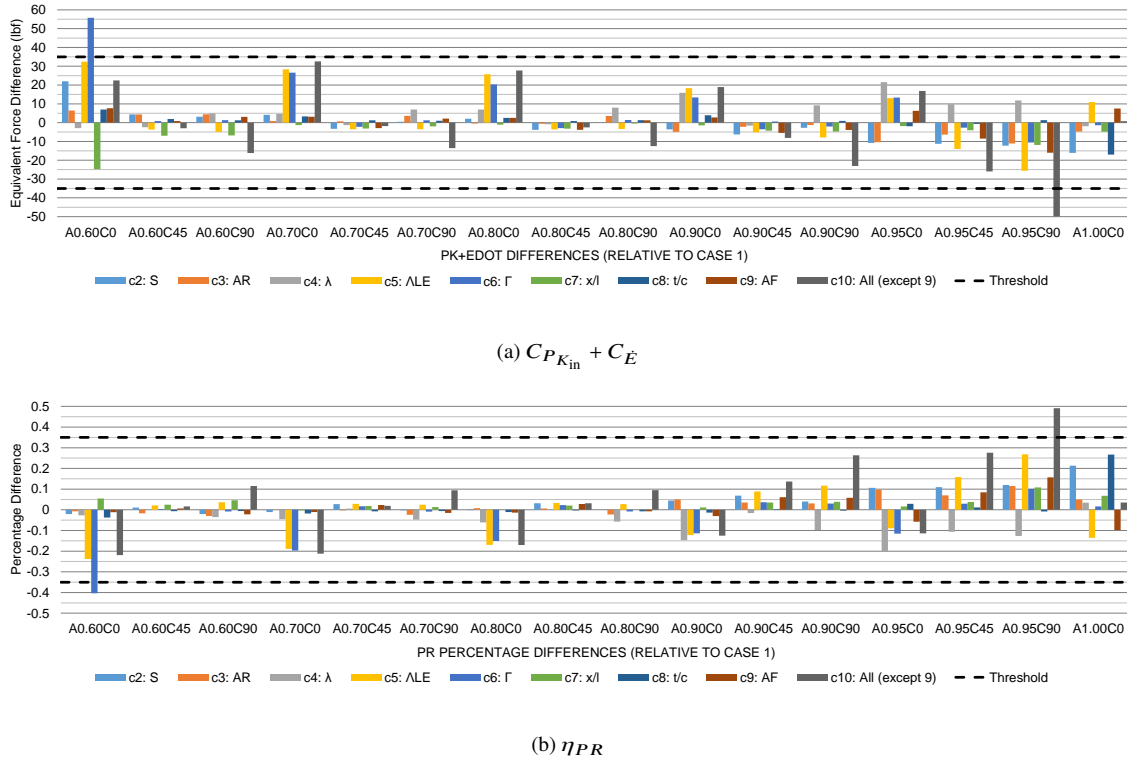
(a) $C_{P_{K_{\text{in}}}} + C_{\dot{E}}$

(b) η_{PR}
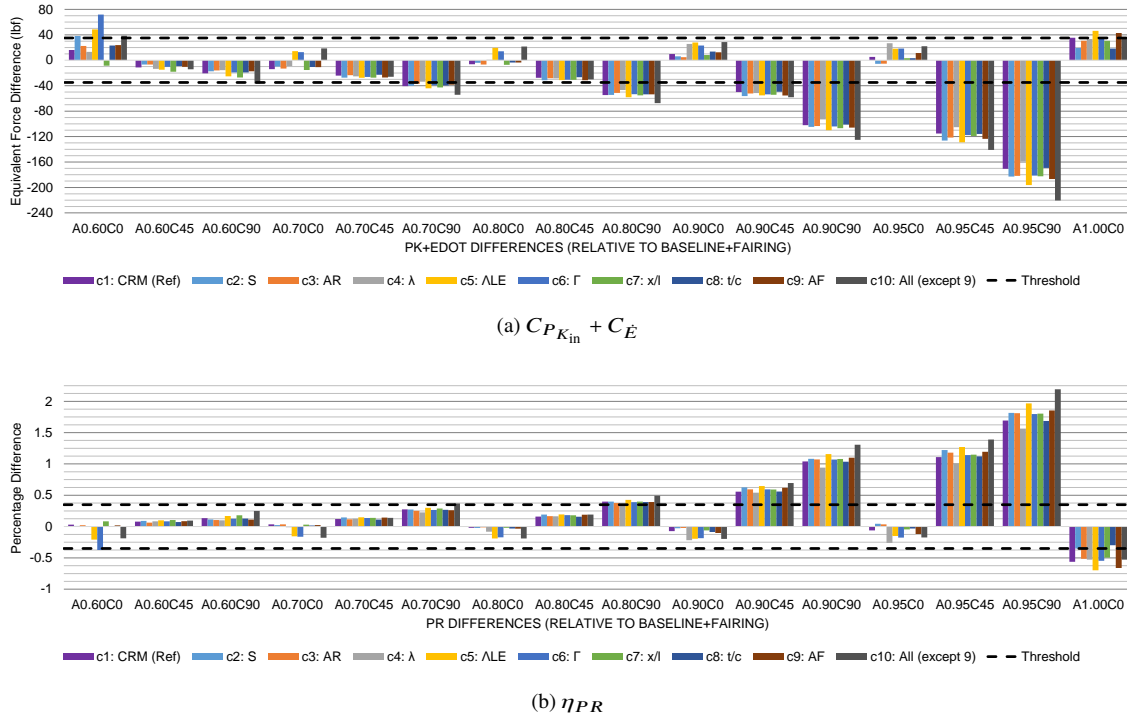
Fig. 26 Experiment 6: influence of the wing on the BLI effects at measurement stations aft of the wing at $\alpha = 2°$. Differences are against the results from fuselage/fairing case 2 in experiment 4

station for the 60% location (A0.6C0), where differences in the BLI effects are strongly influenced by the local flow characteristics in the vicinity of the wing trailing edge. While the results suggest that the wing can be omitted from the geometry model for concepts like the NOVA-BLI, where the engine location falls close to the A0.90C0 and A0.95C0 stations, one must consider this conclusion with caution. There are a few considerations that must be kept in mind when interpreting the obtained results. First, these results are only valid within the design space considered. There is uncertainty in the results if any parameter is set outside the bounds considered in this experiment. Second, even within the perturbation bounds, not all possible combinations of design variables have been tested. Case 10 was run to provide an estimate for how much the result can change when multiple variables are altered at the same time. From these results, it can be inferred that other design combinations should produce comparable results. One cannot guarantee, however, that the BLI effects differences for other design combinations will not exceed the thresholds, especially given how close the maximum difference of 30lbf (at A0.9C0 and A0.95C0) is to the defined threshold of 35lbf. The definition of the threshold itself is dependent on the designer. If the designer wishes to reduce this critical threshold by even 10lbf, the wing then must be included. Lastly, one must not forget about the effects of excessive flow separation on the downstream 0° stations. Conclusions from the results obtained above are only reasonable if the design perturbations stay within this domain of relativity clean flow off the trailing edge. Availability of computational resources and overall run time of CFD with a wing as part of the vehicle geometry model are also important factors to consider. Limited resources may preclude the incorporation of a wing in the CFD geometry model for concepts with an engine position like that on the NOVA-BLI, especially if the differences in the estimates of the BLI effects are too small (based on the designer defined threshold) to justify this additional expense and time. Therefore, it is recommended that inclusion of the wing in the geometry model for such concepts should be left to the discretion of the designer, noting that the discrepancy in the BLI effects by neglecting the wing for such engine locations is much smaller than the error at other circumferential locations.

Relative Sensitivity of BLI Effects to Wing Design Parameters

Fig. 27 compares the differences in the BLI effects for cases 2-10 relative to the reference wing trial 1. A clear pattern is observed at the 60-90% stations where perturbations in the geometry produce noticeable changes at the 0° stations, given that these locations are more sensitive to changes in the wing wake. Just aft of the wing at the A0.6C0 station, Γ and Λ_{LE} have the strongest impact on both $C_{P_{K_{\text{in}}}} + C_{\dot{E}}$ and η_{PR}. The planform area and $\frac{x_{\text{LE}}}{L_{\text{ref}}}$ also have a

28

(a) $C_{P_{K_{\text{in}}}} + C_{\dot{E}}$

(b) η_{PR}

Fig. 27 Experiment 6: relative sensitivity of the BLI effects to the macro and detailed parameters of the wing at $\alpha = 2°$. Differences are relative to the reference wing case (E6.1)

noticeable effect on $C_{P_{K_{\text{in}}}} + C_{\dot{E}}$ at this location. The influence of Γ and Λ_{LE} persists downstream at the $0°$ stations up to the 90% fuselage span station. Thus, the parameters feature in the active variable space for these engine locations. At the 90% span station and aft, the impact of other variables is relatively stronger and determining a dominant parameter is challenging for certain engine locations. At the A0.9C90 station, Λ_{LE} and λ produce differences that are almost double of those produced by other perturbations, except case 10 which is the largest, but the absolute differences relative to the reference wing are still smaller than the threshold. At the A0.95C90 station, the differences relative to the reference wing for most perturbations are larger, but the differences due to Λ_{LE} are still twice as large. At the A1.00 station, the wing $\left(\frac{t}{c}\right)_{\text{max}}$, S, Λ_{LE}, and to a certain extent the airfoil camber are the dominating terms. The significance of the detailed parameters at the A1.00 location is in contrast to the trends observed at other engine locations, where a macro parameter usually had a larger impact. Given the placement and extent of the measurement area at A1.00, this location is influenced strongly by the flow in the vicinity of the wing-fuselage junction. Changes to the wing $\left(\frac{t}{c}\right)_{\text{max}}$ affect the root chord thickness more prominently (given the larger chord length), which in turn affects the flow properties at the A1.00 station. Similar reasoning can be applied to explain the effects of S at A1.00.

At first glance, the results may suggest that since perturbations in the wing design produce differences that are below the critical threshold in most cases, these variations do not need to be kept track of when generating surrogates of the BLI effects. However, this view is misleading. First, the differences shown in Fig. 27 will change if another case from this experiment is picked as a reference. It is thus important to also look at the range of the differences in the BLI effects for each station, given that there is no unique basis for obtaining this reference wing. Calculating the ranges for $C_{P_{K_{\text{in}}}} + C_{\dot{E}}$ and η_{PR} yields values of about 25lbf/0.2% for A0.90C0, 32lbf/0.36% for A0.90C90, 32lbf/0.31% for A0.95C0, 62lbf/0.60% for A0.95C90, and 28lbf/0.40% for A1.00. These ranges indicate that the variability in the BLI effects is significant for top mounted engine locations and for a fuselage trailing edge propulsor. The main takeaway from this experiment is that when designing vehicles with engine locations similar to the D8 and STARC-ABL, not only must the wing be present in the geometry model for the BLI effects surrogate generation, but also, the variability in the wing design parameters must be included. While the BLI effects are more strongly influenced by the the macro parameters of the wing at most engine locations, the impact of detailed parameters like the airfoil camber and thickness is comparable, or even larger, for certain stations such as at A0.95C90 and A1.00.

G. Experiment 7: Sensitivity to Empennage

1. Experimental Overview

The scope of this experiment is restricted to a conventional vertical tail, common to existing aircraft. However, one trial does analyze a t-tail configuration, which is adopted on concepts like the STARC-ABL and the NOVA-BLI, to assess the significance of the horizontal stabilizer. Unlike previous studies, this experiment focuses on the BLI effects calculated at A1.00, since it is directly influenced by the vertical tail. While the BLI version of the CRM [36] places the horizontal tail in front of the A1.00 propulsor, such a configuration is not considered in this experiment for a few reasons. Primarily, it is expected that the interaction between the horizontal tail and propulsor, its effect on the ingested boundary layer, propulsor performance, and aerodynamic efficiency of the stabilizer, will warrant additional design studies to avoid adverse effects. It is thus assumed that concepts featuring a fuselage trailing edge propulsor will place the stabilizer outside the influence of the engine, leading to the t-tail configuration. Additionally, given the similarity between the vertical and horizontal tail, conclusions for the conventional horizontal tail placement can be inferred from the results of the vertical tail studies.

As observed in experiment 3, the shape of the tail cone does have an impact on the BLI effects. To avoid any bias that may occur by integrating a vertical tail on the baseline axisymmetric tail, where, as shown previously, the boundary layer is thicker on the upper side, the tail cone geometry from experiment 3 is used. This tail cone is mated to the baseline fuselage fore section. In the absence of available geometry for a 737-8 like vehicle, the CRM vertical tail designed by Onera [37] is used as a reference geometry. This tail is then scaled down to an area of 20.7m^2 based on an assumed tail volume coefficient of 0.09 (from Raymer [34]) and values of the reference wing area and span in experiment 6. Table 3 shows the main design variables considered, their baseline values, and the perturbed values. Ranges for S_v are driven by the values of the wing planform area considered in experiment 6, for the previously assumed tail volume coefficient. Estimates for the other ranges are obtained from [34].

Table 3   Experiment 7 - Design Variable Settings

Variable	Baseline	Perturbed
Planform Area: S_v	20.77m^2	25m^2
Aspect Ratio: AR_v	1.98	1.2
Taper Ratio: λ_v	0.28	0.60
Leading Edge Sweep: Λ_{LE_v}	44.5°	35°
Max Thickness to Chord: $\left(\frac{t}{c}\right)_{\mathrm{max}}$	13.42%	11.42%
Airfoil Type	NACA 64A013	NACA 0013

The detailed design aspects of vertical tail are the airfoil definitions governed by the airfoil type and thickness $\left(\frac{t}{c}\right)_{\mathrm{max}}$. The other planform variables are the macro parameters. The first trial is the baseline vertical tail geometry, while the following five trials perturb each variable one at a time, keeping the rest at the baseline values. Case 7 represents a vertical tail designed for a t-tail configuration, and is a result of setting the variables at their perturbed values all at once. Case 8 uses the vertical tail from case 7 and adds a horizontal stabilizer, while case 9 is the baseline vertical tail planform with NACA 0013 airfoils instead of those used in the scaled CRM vertical tail. All cases are run at $\alpha = 0°$.

2. Results and Discussion

Fig. 28 presents differences in the BLI effect estimates at the A1.00 station for each of the nine cases, relative to the no vertical tail baseline geometry from experiment 3.1. Fig. 29 compares the η_{PR} contours between the no tail baseline and the reference tail (E7.1) at the A1.00 station, highlighting the fuselage boundary layer and vertical tail wake. The wake of the vertical tail and the outward deflection of the boundary layer in y direction help increase $C_{P_{K_{\mathrm{in}}}}$ and decrease $C_{\dot{E}}$ and η_{PR} relative to the no tail baseline. The higher static pressure aft of the tail, relative to the no-tail case, increases the magnitude of the pressure defect work rate component of $C_{\dot{E}}$, effectively offsetting the kinetic energy defect rate benefit in the vertical tail wake, resulting in a net decrease in $C_{\dot{E}}$. While the differences in $C_{\dot{E}}$ are smaller than the critical threshold, the net effect of $C_{P_{K_{\mathrm{in}}}} + C_{\dot{E}}$ still exceeds the threshold given the stronger favorable impact of the wake on $C_{P_{K_{\mathrm{in}}}}$, as seen in Fig. 28. The differences in η_{PR} also exceed the threshold. The main conclusion from Fig. 28 is that a vertical tail must be included when calculating the BLI effects for a STARC-ABL like concept.

(a) $C_{P_{K_{\text{in}}}}$

(b) $C_{\dot{E}}$

(c) $C_{P_{K_{\text{in}}}} + C_{\dot{E}}$
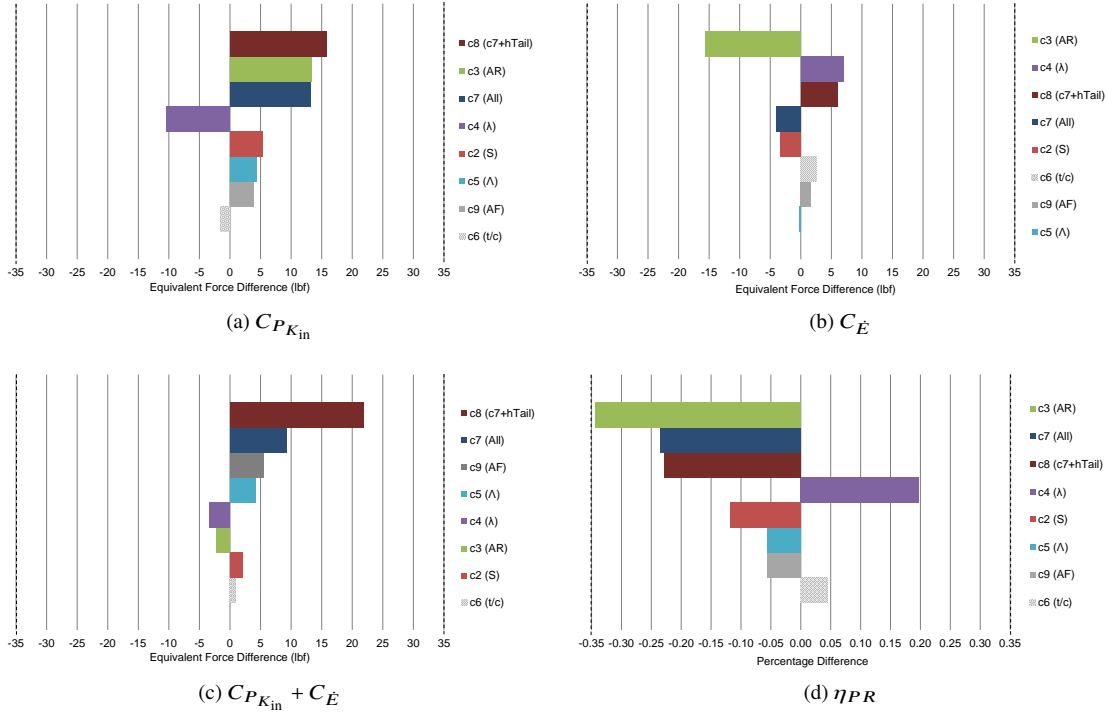
(d) η_{PR}
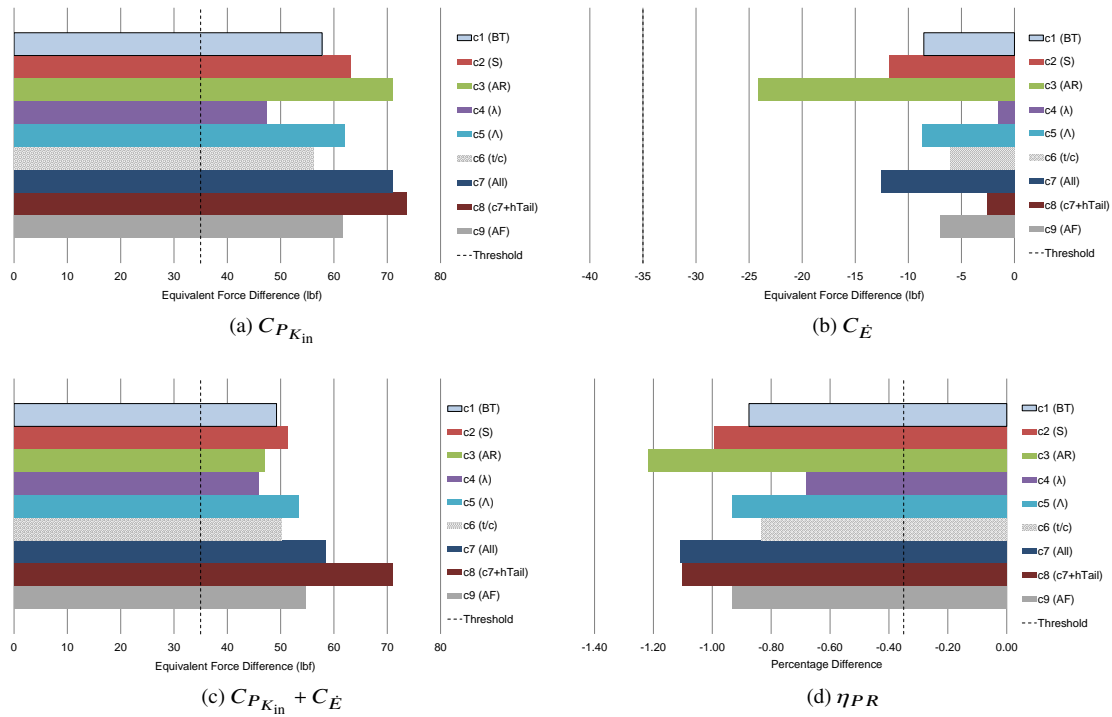
Fig. 28   Experiment 7: differences in BLI effects at A1.00 due to changes in tail design, relative to E3.1

To assess the significance of the design changes on the BLI effects, Fig. 30 ranks the differences between cases 2-9 relative to the reference tail in case 1. A few observations can be made from the presented results. Firstly, all differences relative to the baseline vertical tail are below the critical threshold, for the given ranges in the design variables. Even case 7, where all parameters (except airfoil type) are set at the perturbed values, falls below the critical threshold for all BLI effects. Variations in the pressure recovery are more significant for cases 3, 4, 7, and 8 and follow expected trends given the behavior of the vertical wake extent based on the geometry. Any configuration that tends to produce a thicker
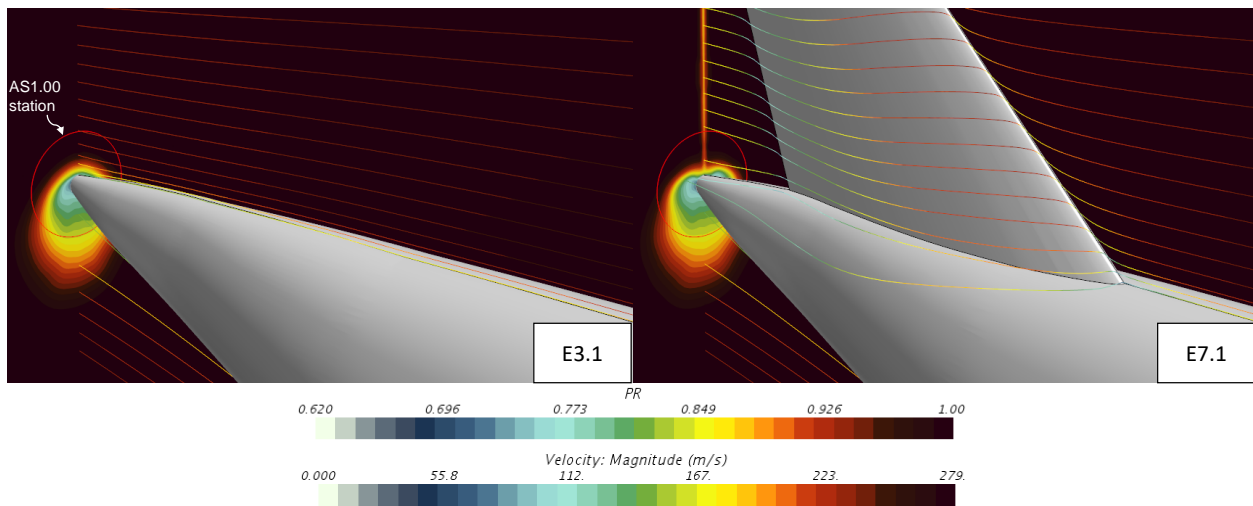
Fig. 29   Experiment 7: effects of the vertical tail on the flow streamlines (at symmetry plane) and the A1.00 boundary layer. The streamlines are colored based on the velocity magnitude

(a) $C_{P_{K_{\text{in}}}}$

(b) $C_{\dot{E}}$

(c) $C_{P_{K_{\text{in}}}} + C_{\dot{E}}$

(d) η_{PR}

Fig. 30   Experiment 7: differences in BLI effects at A1.00 due to changes in tail design, relative to E7.1

wake, such as a low aspect ratio tail, will have a lower pressure recovery. Reducing the tail $\left(\frac{t}{c}\right)_{\text{max}}$ and increasing λ_v both decrease the overall thickness of the wing in the region just in front of the A1.00 integration area, producing a thinner wake and thus improving η_{PR}.

With regards to the relative significance of the parameters, it can be observed from the BLI effects plots in Figs. 30a, 30b, and 30d that the detailed parameters like airfoil type and $\left(\frac{t}{c}\right)_{\text{max}}$ have a smaller impact on the BLI effects than the macro parameters, within the defined ranges. Also, comparing case 7 and case 8, noting that both have the same vertical tail, the effective contribution of the horizontal stabilizer on $C_{P_{K_{\text{in}}}}$ is approximately 2.6 lbf, and 0.008% on η_{PR}. The impact on $C_{\dot{E}}$ is larger, and the net effect on $C_{P_{K_{\text{in}}}} + C_{\dot{E}}$ is around 12.6 lbf. On the individual BLI effects, AR_v, λ_v, and S_v are the most significant macro parameters. The range in $C_{P_{K_{\text{in}}}} + C_{\dot{E}}$ differences is only about 12lbf for just the vertical tail. However, the largest variation seen in the η_{PR} differences is about 0.54%, when comparing case 3 to case 4, which exceeds the critical threshold. Recall that the range in η_{PR} variation due to wing parameter changes for the A1.00 station was 0.40%. The combined effect of the wing and the tail geometry variations can have a substantial impact on the BLI effects estimates. Thus, it is recommended that the vertical tail design variables be included in the BLI effects surrogate models. A computational cost effective option is to only vary the most significant macro parameters, i.e., AR_v, λ_v, and S_v, defaulting the airfoil to a reasonable type and thickness. Doing so would minimize the number of runs required to cover the sample space. While the impact of the horizontal tail on the flow is expected to be more significant if it is lowered, for the location tested, the stabilizer can be neglected.

H. Experiment 8: Sensitivity to Inlet Ramp

1. Experimental Overview

Most BLI concepts feature an S-shaped inlet feeding into the propulsor. This shape can be crudely parameterized by one macro parameter and two detailed parameters, as illustrated in Fig. 31. In this figure, the inlet ramp is defined between two fuselage cross sectional stations, shown in gray. The end station corresponds to the nacelle highlight plane of the fictitious propulsor. The inlet angle (macro parameter) is the angle created by the cross sectional area change between the start and end station. The detailed skinning angles, shown in blue, control the slopes of the spline curve connecting the start and end points of the inlet. The inlet and skinning angles are defined with reference to the
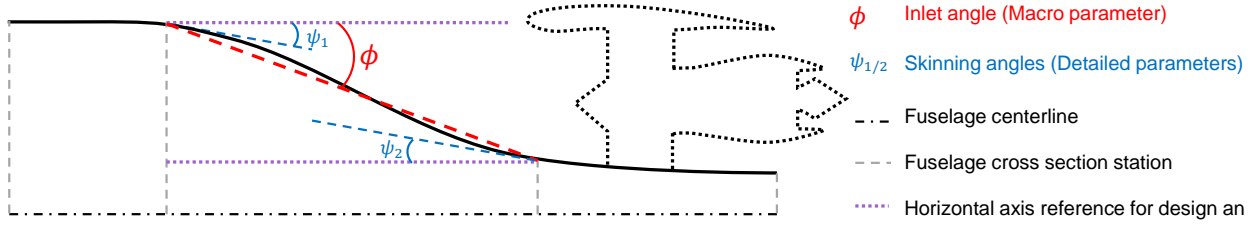
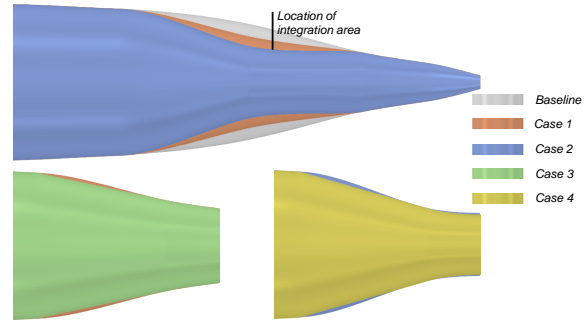**Fig. 31 Parameterization of an S-shaped BLI inlet geometry**

horizontal axis shown in purple. The simplest geometry is a linear ramp, where $\psi_i = \phi$, resulting in sharp corners at the start and end points. By controlling the values of ψ_i, the designer can alter the curvature at these locations, thereby changing the shape of the S curve from a linear to a non-linear ramp. The design variables chosen allow for an efficient experimentation process to assess the sensitivity of the BLI effects to the major design aspects of the inlet.

Table 4 Experiment 8: Overview of Cases

Experiment	ϕ (°)	ψ_1 (°)	ψ_2 (°)	Comments
2.8-1	12	2.00	11.74	
2.8-2	16	2.00	11.74	$\Delta\phi = 4°$
2.8-3	12	12	12	Linear ramp
2.8-4	16	16	16	Linear ramp

The starting geometry used for this experiment is the one from E3.1, where the notional 737-8 tail cone was used in conjunction with the baseline fore-body. The measurements for the BLI effects are obtained at the 85% axial, 0° circumferential station, and is thus a notional model of the NOVA-BLI concept. The baseline values for the macro and detailed parameters are: $\phi = 6.71°$, $\psi_1 = 2.00°$, $\psi_2 = 11.74°$, where the angles are defined as shown in Fig. 31. This geometry is modified to create four different inlet shapes.

Table 4 presents the four cases that are run, visually compared in Fig. 32. Cases 1 and 2 are compared to quantify the differences in the BLI effects due to a four degree change in the inlet angle. Cases 3 and 4 are linear ramp approximations of cases 1 and 2, attempting to quantify the impact this simplest representation has on the BLI effects, by comparing the results to cases 1 and 2 respectively. From basic aerodynamics knowledge, and the results of experiment 3, the adverse characteristics of sharp corners in subsonic flows is well established. However, these cases can be considered as a reasonable lower bound in the scale of design detail, where any curvature enhances the level of detail. Cases 3 and 4 thus serve to establish how much a designer can get away with

Fig. 32 Experiment 8: top view of inlet shapes. Integration area is located at A0.85C0

by making this crude approximation. If small, the need for determining the curvature is unnecessary in concept design, as this can be left as an OML refinement exercise in preliminary design. If large, a suitable middle ground needs to be found where defaulting such curvature has a minimal impact on the results.

2. Results and Discussion

Fig. 33 presents the differences in the BLI effects due to changes in the macro and detailed parameters. Blue bars denote changes due to the macro parameter, while gray bars depict the impact of perturbations to the detailed parameters. It is evident that the differences in all three BLI effects due to the change in the macro parameter are much larger than the differences due to the changes in the detailed parameters. The impact of the macro parameter change exceeds the critical thresholds, while the influence of the detailed parameters is below the critical thresholds.

It appears that the significance of the inlet ramp curvature is dependent on the setting for the inlet ramp angle. For the ramp angle of 12°, the impact of curvature change (C3-C1) is minimal. For a steeper inlet ramp angle, the curvature influence on the BLI effects is more pronounced, albeit within the critical thresholds. Fig. 34 compares the Mach contours for each of the cases. Comparing case 1 to 3, one case see that switching to a sharp corner produces localized

(a) Relative differences in $C_{P_{K_{\text{in}}}}$ and $C_{\dot{E}}$

(b) Percentage difference in η_{PR}
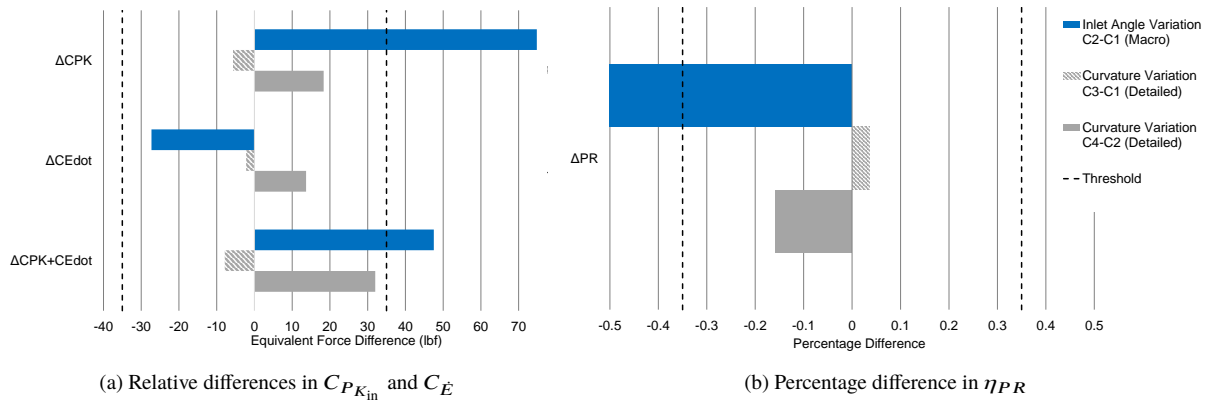
Fig. 33   Experiment 8: differences in BLI effects from changes in inlet design

flow acceleration, consistent with observations from experiment 3. In this instance however, the impact on the boundary layer downstream is minimal, as seen in Fig. 35. Given the flow acceleration over the corner, the resulting boundary layer downstream is slightly thinner in case 3, accounting for the decrease in $C_{P_{K_{\text{in}}}}$ and $C_{\dot{E}}$ and increase in η_{PR} seen in Fig. 33. However, in case 4, a small separation bubble is formed just after the corner, highlighted in Fig. 34. This bubble alters the effective body shape seen by the flow and thus has a more noticeable impact on the ingested boundary layer downstream, as seen by the bulge in the η_{PR} contours for case 4 in Fig. 35. Also evident from the Mach and η_{PR} contours in Figs. 34 and 35 is the thicker boundary layer as a result of increasing the inlet ramp angle, which explains the increase in $C_{P_{K_{\text{in}}}}$ and decrease in η_{PR} in case 2 relative to case 1.

For smaller inlet angles, the concept designer can likely get away with a simple linear ramp in the CFD geometry model. For larger ramp angles, however, this approximation may result in more substantial discrepancies in the BLI effects estimates relative to the results that are expected at the end of the preliminary design stage refinement.
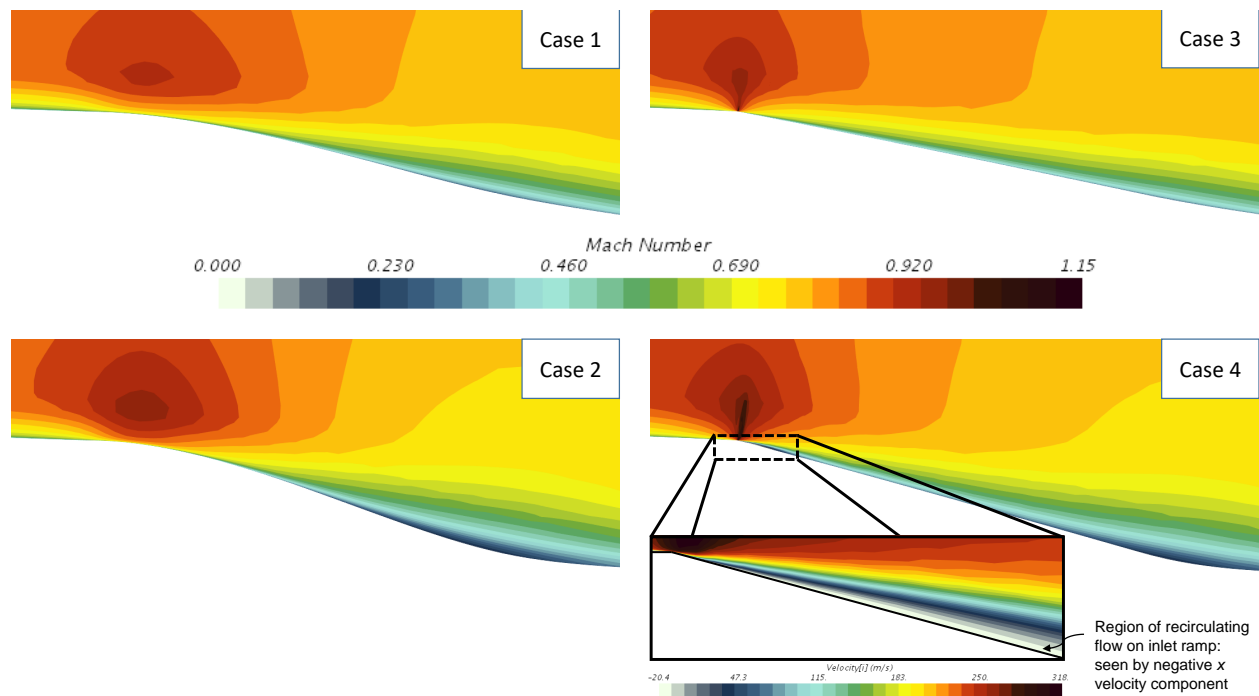
Fig. 34   Experiment 8: Mach contours at the inlet center-plane
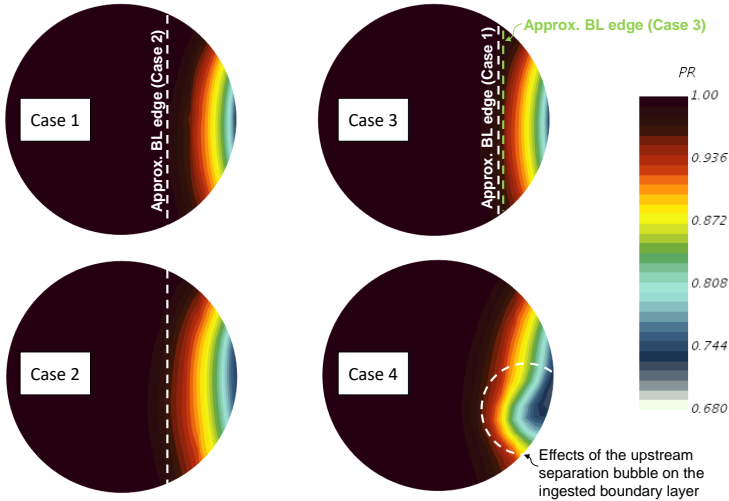
Fig. 35 Experiment 2.8: η_{PR} contours for the ingested boundary layer at 85% axial distance along the fuselage

Recognizing that the inlet ramp OML will be subject to optimization in the later stages of design, it is recommended that the concept designer focus on the inlet ramp angle. The skinning angles should be set to some reasonable value such that no excessive separation is observed at the design conditions at which the BLI effects surrogate models will be generated. While this curvature may not be optimal, the results above suggest that the discrepancy between the concept design model and the optimized design will be small, as long as the macro parameter is the same. This is because the BLI effects are more sensitive to the macro parameters in this instance, as hypothesized. If the inlet ramp angle is unknown, it should be varied for the surrogate models.

VI. Conclusions

An integral part of a parametric BLI concept design methodology is the formulation of surrogate models of the BLI effects as a function of airframe geometry. However, as discussed in Sec. II, general comments on the sensitivity of the boundary layer properties to the airframe design could not be found in the reviewed literature. As such, a question was posed regarding what features of the airframe design needed to be considered as part of this surrogate modeling process and which ones could be defaulted. Based on theoretical considerations covered in Sec. III, a hypothesis was formed, which can be broken down into three main points:

1) The engine axial and circumferential location on the fuselage plays a role in determining how much a given design feature contributes to the BLI effects measured at that location. To elaborate:
    1) Small perturbations to the flow (no shocks/separation), as a result of modifications to the geometry, decay along the axial distance in the zone of influence. In other words, small flow perturbations are local effects.
    2) The wing impact on the BLI effects varies based on the circumferential location of the engine
2) The BLI effects are more sensitive to changes in the macro parameters of airframe, in general, than to changes in the detailed parameters. This aspect is tied to the condition that no shocks or flow separation results from these changes in detailed variables. Such adverse flow characteristics have a global influence on the BLI effects.
3) Any variable present in the inactive variable space need not be considered in the surrogate model formulation. Additionally, detailed parameters that fall in the active variable space may also be defaulted to reasonable settings in concept design, under certain guidelines. The resulting difference in BLI effects estimates is smaller than the discrepancy caused by defaulting an active macro variable, under the assumption that point 2 above is true.

A series of experiments was designed to test the different aspects of the hypothesis. Results from experiment 2 support points 1.1, 2 and 3. The nose geometry parameters feature in the inactive variable set for a shock free perturbation of the nose. However, when the detailed parameters are defaulted to values that produced a shock, the impact of this large perturbation is felt at all axial stations. Experiment 3 verifies points 2 and 3. The tail closure and upsweep angles have a stronger impact on the BLI effects than the changes in curvature between the tail cone and center-body. Point 1.1 is largely supported by the results from experiment 4, except at $\alpha = 2°$, where the results at A1.00 exceeded the threshold. Changes to the fuselage shape, in experiment 5, are found to have a smaller impact in general, than modifications to the fuselage length and cross sectional area, supporting points 2 and 3. The circular approximation for the D8 cross section is an example of when the fuselage shape variables fall under the active space, however, the differences observed are actually related to the macro parameters of the tail cone. Results from experiment 6 clearly highlight point 1.2, where a distinct variation in the BLI effects is noticed based on engine location. A consequence of this trend is that when designing concepts with side mounted engines, the penalty of neglecting the wing in the geometry model is much smaller than for concepts with engine locations similar to the D8 and the STARC-ABL. With regards to

the detailed and macro parameters of the wing, results at some engine locations support point 2, but for others such as at A1.00, sensitivity of the BLI effects to the two variable classes is comparable. For vertical tail, the results support points 2 and 3, highlighting that variations in the airfoil definition are less significant than the changes in other macro parameters. Thus, the airfoils can be defaulted for a smaller design space. Lastly, results from experiment 8 show that the inlet angle has a more significant impact than the detailed skinning angles, verifying points 2 and 3.

In summary, the experiments answer the overarching research question, filling the void in literature by identifying the critical airframe design space and showing how it changes based on the engine location, for tube and wing BLI concepts. These findings reduce the dimensionality of the airframe design space and facilitate the generation of BLI effects surrogate models using CFD in concept design. These models can then incorporated in the coupled aero-propulsive BLI vehicle sizing, engine cycle design, and optimization methodology currently under development.

References

[1] Felder, J. L., Kim, H. D., and Brown, G. V., "Turboelectric Distributed Propulsion Engine Cycle Analysis for Hybrid-Wing-Body Aircraft," *47th AIAA Aerospace Sciences Meeting including the New Horizons Forum and Aerospace Exposition*, AIAA, 2009. doi:10.2514/6.2009-1132.

[2] Felder, J. L., Kim, H. D., Brown, G. V., and Chu, J., "An Examination of the Effect of Boundary Layer Ingestion on Turboelectric Distributed Propulsion Systems," *49th AIAA Aerospace Sciences Meeting including the New Horizons Forum and Aerospace Exposition*, AIAA, 2011. doi:https://doi.org/10.2514/6.2011-300.

[3] Welstead, J. R., and Felder, J. L., "Conceptual Design of a Single-Aisle Turboelectric Commercial Transport with Fuselage Boundary Layer Ingestion," *AIAA SciTech Forum*, AIAA, 2016. doi:10.2514/6.2016-1027.

[4] Greitzer, E. M., Bonnefoy, P. A., De la Rosa Blanco, E., Dorbian, C., Drela, M., and Hall, D. K., "N+3 Aircraft Concept Designs and Trade Studies, Final Report," Report, NASA Glenn Research Centre, 2010.

[5] Drela, M., "Development of the D8 Transport Configuration," *AIAA Applied Aerodynamics Conference*, AIAA, 2011.

[6] Yutko, B., Titchener, N. A., Courtin, C., Lieu, M. K., Wirsing, L., Tylko, J., Chambers, J., Roberts, T., and Clint, C., "Conceptual Design of a D8 Commercial Aircraft," *AIAA Aviation Forum*, AIAA, 2017.

[7] Wiart, L., Atinault, O., Grenon, R., Paluch, B., and Hue, D., "Development of NOVA Aircraft Configurations for Large Engine Integration Studies," *33rd AIAA Applied Aerodynamics Conference*, AIAA, 2015.

[8] Florea, R. V., Matalanis, C., Hardin, L. W., Stucky, M., and Shabbir, A., "Parametric Analysis and Design for Embedded Engine Inlets," *48th AIAA/ASME/SAE/ASEE Joint Propulsion Conference & Exhibit*, AIAA, 2012.

[9] Hardin, L. W., Tillman, G., Sharma, O. P., Berton, J., and Arend, D. J., "Aircraft System Study of Boundary Layer Ingesting Propulsion," *48th AIAA/ASME/SAE/ASEE Joint Propulsion Conference & Exhibit*, AIAA, 2012.

[10] Liu, C., Doulgeris, G., Laskaridis, P., and Singh, R., "Thermal cycle analysis of turboelectric distributed propulsion system with boundary layer ingestion," *Aerospace Science and Technology*, Vol. 27, No. 1, 2013, p. 8.

[11] Lee, B. J., Liou, M.-S., and Kim, C., "Optimizing a Boundary-Layer-Ingestion Offset Inlet by Discrete Adjoint Approach," *AIAA Journal*, Vol. 48, No. 9, 2010. doi:10.2514/1.J050222.

[12] Kenway, G. K., and Kiris, C., "Aerodynamic Shape Optimization of the STARC-ABL Concept for Minimal Inlet Distortion," *AIAA SciTech Forum*, AIAA, 2018. doi:10.2514/6.2018-1912.

[13] Gray, J. S., Mader, C. A., Kenway, G. K., and Martins, J. R. R. A., "Modeling Boundary Layer Ingestion Using a Coupled Aeropropulsive Analysis," *Journal of Aircraft*, Vol. 55, No. 3, 2018. doi:10.2514/1.C034601.

[14] Gray, J. S., and Martins, J. R. R. A., "Coupled Aeropropulsive Design Optimization of a Boundary Layer Ingestion Propulsor," *The Aeronautical Journal*, 2018, p. 19.

[15] Pokhrel, M., Shi, M., Ahuja, J., Gladin, J. C., and Mavris, D. N., "Conceptual Design of a BLI Propulsor Capturing Aero-Propulsive Coupling and Distortion Impacts," *AIAA SciTech Forum*, AIAA, 2019.

[16] Wang, K. C., "On the Determination of the Zones of Influence and Dependence for Three-Dimensional Boundary-Layer Equations," *Journal of Fluid Mechanics*, Vol. 8, No. 2, 1971, pp. 397–404.

[17] McLean, J. D., *Understanding Aerodynamics : Arguing from the Real Physics*, John Wiley Sons, Incorporated, 2012.

[18] Gray, J. S., Kenway, G. K., Mader, C. A., and Martins, J. R. R. A., "Aeropropulsive Design Optimization of a Turboelectric Boundary Layer Ingestion Propulsion System," *Aviation 2018*, AIAA, 2018. doi:10.2514/6.2018-3976.

[19] Drela, M., "Power Balance in Aerodynamic Flows," *AIAA Journal*, Vol. 47, No. 7, 2009.

[20] Sato, S., "The Power Balance Method for Aerodynamic Performance Assessment," Thesis, 2012.

[21] Hall, D. K., Huang, A. C., Uranga, A., Greitzer, E. M., Drela, M., and Sato, S., "Boundary Layer Ingestion Propulsion Benefit for Transport Aircraft," *Journal of Propulsion and Power*, Vol. 33, No. 5, 2017.

[22] Arntz, A., "Civil Aircraft Aero-thermo-propulsive Performance Assessment by an Exergy Analysis of High-fidelity CFD-RANS Flow Solutions," Thesis, 2014.

[23] Hall, D. K., Lieu, M. K., and Drela, M., "Aerodynamic Performance Accounting for Ultra-Integrated Air Vehicle Configurations," *AIAA SciTech Forum*, AIAA, 2019.

[24] Boeing, "737 MAX Airplane Characteristics for Airport Planning (Rev. B)," Report, Boeing Commercial Airplanes, 2018.

[25] Teal, M., "New 737 MAX: Improved Fuel Efficiency and Performance," *Boeing AERO Magazine, Q1 2014*, , No. 53, 2014.

[26] Liou, M.-S., "A Sequel to AUSM: AUSM+," *Journal of Computational Physics*, Vol. 129, 1996.

[27] Menter, F. R., "Two-Equation Eddy-Viscosity Turbulence Models for Engineering Applications," *AIAA Journal*, Vol. 32, No. 8, 1994.

[28] Kirby, R., Michelle, and Mavris, D. N., "The Environmental Design Space," *28th International Congress of the Aeronautical Sciences*, ICAS, 2008.

[29] Schutte, J., Tai, J., Sands, J. S., and Mavris, D. N., "Cycle Design Exploration Using Multi-Design Point Approach," *ASME Turbo Expo 2012: Turbine Technical Conference and Exposition*, ASME, 2012. doi:10.1115/GT2012-69334.

[30] Ordaz, I., Rallabhandi, S., Nielsen, E. J., and Diskin, B., "Mitigation of Engine Inlet Distortion through Adjoint-Based Design," *AIAA AVIATION Forum*, AIAA, 2017.

[31] Airbus, "A350 Aircraft Characteristics Airport and Maintenence Planning," Report, Airbus SAS, 2019.

[32] Vassberg, J. C., DeHaan, M. A., Rivers, S. M., and Wahls, R. A., "Development of a Common Research Model for Applied CFD Validation Studies," *Applied Aerodynamics Conference*, AIAA, 2008.

[33] Suleman, A., Alonso, F., Vale, J., Oliveira, E., and Lau, F., "Non-Linear Aeroelastic Analysis in the Time Domain of High-Aspect-Ratio Wings: Effect of Chord and Taper-Ratio Variation," *The Aeronautical Journal*, Vol. 121, No. 1235, 2017, p. 33.

[34] Raymer, D. P., *Aircraft Design: A Conceptual Approach*, 5th ed., AIAA, Reston, VA, 2012.

[35] Kulfan, B. M., "Universal Parametric Geometry Representation Method," *Journal of Aircraft*, Vol. 45, No. 1, 2008.

[36] Blumenthal, B. T., Elmiligui, A. A., Geiselhart, K. A., Campbell, R. L., Maughmer, M. D., and Schmitz, S., "Computational Investigation of a Boundary-Layer Ingesting Propulsion System for the Common Research Model," *46th AIAA Fluid Dynamics Conference*, AIAA, 2016. doi:10.2514/6.2016-3812.

[37] Atinault, O., and Hue, D., "Design of a Vertical Tail for the CRM Configuration," Report, Onera, 2014.